Aerospace Science and Technology 135 (2023) 108201

Contents lists available at ScienceDirect

Aerospace Science and Technology

journal homepage: www.elsevier.com/locate/aescte

Stability and control issues of multirotor suspended load transportation: An analytical closed–form approach

Emanuele L. de Angelis *, Fabrizio Giulietti

University of Bologna, Department of Industrial Engineering (DIN), CIRI Aerospace, Forlí, 47121, Italy

ARTICLE INFO

Article history:
Received 5 October 2022
Received in revised form 20 December 2022
Accepted 15 February 2023
Available online 21 February 2023
Communicated by Christian Circi

ABSTRACT

In the present paper a fully–analytical framework is outlined to analyze the effects of cable–suspended loads on multirotor platforms. In particular, the dynamics of an isolated vehicle is first investigated by including the complete model of the electric propulsion system. Then, system description is extended to the load, which introduces non–actuated degrees of freedom and is suspended through a linear–elastic cable. In order to provide the complete slung–load system with a closed–loop desired behavior, an auxiliary controller is proposed to recover or improve the initial multirotor dynamic properties, while stabilizing load oscillations. To this end, closed–form equations are derived to design the auxiliary controller gains, based on the knowledge of a limited set of parameters. A test case is proposed relative to a commercial–off–the–shelf hexarotor whose electrical propulsion system has been characterized by an experimental campaign performed at University of Bologna premises.

1. Introduction

There is an increasing interest in the use of both manned and highly–automated unmanned rotorcraft to carry payloads, envisaging complex Air Mobility and Delivery (AMD) scenarios, with significant benefits in the fields of cargo transportation, sensor deployment, fire fighting, and construction [1,2]. In this respect, two approaches are typically considered. The first one consists in equipping the lifting vehicle with graspers or a sufficiently large cargo compartment, leading to increased take–off mass, complexity, and cost. With regard to vehicle performance, flight endurance and range would be typically degraded and attitude dynamics would suffer from reduced agility [3,4]. The second approach consists in the equipment of cable–suspended loads, which relatively preserves the performance of the aircraft and the simplicity of systems, but it introduces additional non–actuated degrees of freedom [5,6]. When carrying a suspended payload, in fact, rotorcraft motion and/or external disturbances induce cable swing. On the one hand, the payload creates disturbance forces and moments that can significantly affect the motion of the vehicle. On the other hand, the oscillations can damage the payload or its environment by colliding with obstacles. To this aim, different control strategies are available in the literature for both conventional helicopter and multirotor configurations. As an example, an adaptive controller is proposed in [7] to cope with changes to the multirotor center of gravity. In [8] the cable is modeled as a series of interconnected links and a nonlinear geometric controller is derived to asymptotically stabilize the position of the vehicle and keep the cable in its vertical position. In [9] a quadrotor platform with a cable–suspended load is described in terms of a differentially–flat hybrid system in order to address cable collapse. In such a framework, a controller regulating the aircraft attitude and the position of the load on a vertical plane is finally derived. In [10] the nonlinear model of the system is decoupled into two subsystems: the inner loop describes vehicle rotational dynamics and attitude state variables are used as an input to the outer loop, related to the remaining state variables. A nested saturation controller is finally derived for stabilizing both the aircraft and the suspended load. Input–shape filtering methods are also used to generate a reference trajectory that minimizes residual swing during maneuvers [11]. An inverse simulation approach based on an integration method is proposed in [12] to determine the necessary control action that allows a quadrotor platform to track a prescribed trajectory. In such a case, the effect of drag on the payload is included in the model, which becomes a fundamental feature when the vehicle is used for towing a payload immersed in water. Finally, in a recent work by some of the authors [13], a nonlinear controller is proposed with the aim to ensure simultaneous trajectory–tracking and payload swing damping, according to a point–mass modeling of both the rotorcraft and the load. In particular, the structure of the controller is chosen so that the coupled slung–load system exhibits

* Corresponding author.
E-mail addresses: emanuele.deangelis4@unibo.it (E.L. de Angelis), fabrizio.giulietti@unibo.it (F. Giulietti).

https://doi.org/10.1016/j.ast.2023.108201

Nomenclature

$\mathbf{0}_q$	null matrix with dimension q
A	rotor disc area ... m^2
a	blade airfoil lift curve slope ... rad^{-1}
a_0	rotor pre–cone angle ... rad
A_1, A_2, A_3	rotorcraft frame drag areas ... m^2
A_c	payload reference area ... m^2
b	multirotor arm length ... m
BL	buttline ... m
$\boldsymbol{c}$	payload position with respect to H ... m
c_{75}	blade chord at 75% radius ... m
C_d	drag coefficient
CG	rotorcraft center of gravity
CP	rotorcraft frame center of pressure
C_T	rotor thrust coefficient
e	error with respect to the desired condition
$\mathcal{F}_B$	rotorcraft body–fixed frame
$\mathcal{F}_E$	Earth–fixed frame
$\mathcal{F}_H$	local–vertical local–horizontal frame
$\mathcal{F}_S$	rotorcraft structural frame
H	hook point
$\boldsymbol{h}$	$=[h_1, h_2, h_3]^T$ hook point position ... m
$\boldsymbol{I}_q$	identity matrix with dimension q
$\boldsymbol{J}$	$=diag\,(J_1, J_2, J_3)$ rotorcraft inertia matrix ... kg m^2
K	cable Hooke's constant ... N m^{-1}
k_{ir}, k_{p_r}	sample inner controller gains (yaw rate error)
k_{iv}, k_{p_v}	sample inner controller gains (vertical speed error)
$k_{i\phi}$, k_{p_ϕ}, k_p	sample inner controller gains (roll angle error)
$k_{i\theta}$, k_{p_θ}, k_q	sample inner controller gains (pitch angle error)
$\bar{k}_{i_r}$, $\bar{k}_{p_r}$	auxiliary controller gains (yaw rate error)
$\bar{k}_{i_v}$, $\bar{k}_{p_v}$	auxiliary controller gains (vertical speed error)
$\bar{k}_{i_\phi}$, $\bar{k}_{p_\phi}$, $\bar{k}_p$	auxiliary controller gains (roll angle error)
$\bar{k}_{i_\theta}$, $\bar{k}_{p_\theta}$, $\bar{k}_q$	auxiliary controller gains (pitch angle error)
$\bar{k}_{\eta_1}$, $\bar{k}_{\eta_2}$, $\bar{k}_{\nu_1}$, $\bar{k}_{\nu_2}$	auxiliary controller gains (payload position error)
k_{ind}	induced power coefficient
k_Q	torque model coefficient ... N m s^2 rad^{-2}
k_T	thrust model coefficient ... N s^2 rad^{-2}
k_Ω	ESC model coefficient
L	cable nominal length ... m
m	rotorcraft mass ... kg
m_c	payload mass ... kg
N	number of rotors
n	ESC model exponent
n_b	number of rotor blades
$\boldsymbol{p}$	$=[x, y, z]^T$ rotorcraft position ... m
PWM	Pulse Width Modulation signal ... µs
Q	rotor torque ... N m
R	rotor radius ... m
Re	blade Reynolds number at 75% radius
STA	stationline ... m
S	maximum overshoot
T	rotor thrust ... N
t_o	time of maximum overshoot ... s
t_r	rise time ... s
t_s	settling time ... s
$\boldsymbol{T}_{BE}$	Coordinate transformation matrix between $\mathcal{F}_E$ and $\mathcal{F}_B$
$\boldsymbol{T}_{HE}$	Coordinate transformation matrix between $\mathcal{F}_E$ and $\mathcal{F}_H$
$\boldsymbol{v}$	$=[u, v, w]^T$ rotorcraft linear velocity ... m s^{-1}
V_{75}	blade speed at 75% radius ... m s^{-1}
v_i	rotor induced speed ... m s^{-1}
V_{tip}	blade tip speed ... m s^{-1}
WL	waterline ... m
$\boldsymbol{x}_B$, $\boldsymbol{y}_B$, $\boldsymbol{z}_B$	rotorcraft body–fixed frame axes
$\boldsymbol{x}_E$, $\boldsymbol{y}_E$, $\boldsymbol{z}_E$	Earth–fixed frame axes
$\boldsymbol{x}_H$, $\boldsymbol{y}_H$, $\boldsymbol{z}_H$	local–vertical local–horizontal frame axes
$\boldsymbol{x}_S$, $\boldsymbol{y}_S$, $\boldsymbol{z}_S$	rotorcraft structural frame axes

Greek symbols

δ	throttle signal ... µs
ε	time integral of error e
$\boldsymbol{\eta}$	$=[\eta_1, \eta_2, \eta_3]^T$ payload position error ... m
θ_0	blade root pitch angle ... rad
θ_t	blade twist angle (tip minus root pitch angle) ... rad
λ, $\bar{\lambda}$	prescribed eigenvalues
μ	air dynamic viscosity ... Pa s
$\boldsymbol{\nu}$	$=[\nu_1, \nu_2, \nu_3]^T$ payload velocity error ... m s^{-1}
ξ	controller weight parameter
ρ	air density ... kg m^{-3}
σ	rotor solidity
χ	density scaling parameter
ψ, θ, ϕ	3-2-1 Euler angle sequence ... rad
Ω	rotor angular rate ... rad s^{-1}
$\boldsymbol{\omega}$	$=[p, q, r]^T$ rotorcraft angular velocity ... rad s^{-1}

Subscripts

c	cable–related variable
d	desired value
E	vector components in $\mathcal{F}_E$
exp	value obtained through experiments
fwd	feed–forward term
H	vector components in $\mathcal{F}_H$
$idle$	idle condition
j	variable related to the j–th rotor
max	maximum value
$pitch$	variable related to the pitch channel
$roll$	variable related to the roll channel
v	variable related to the vertical channel
yaw	variable related to the yaw channel

Superscripts

(a)	aerodynamic force/moment contribution
(aux)	auxiliary controller contribution
(c)	cable–related force/moment contribution
(f)	rotorcraft frame force/moment aerodynamic contribution
(g)	gravity force contribution
(inn)	inner controller contribution
(r)	rotor force/moment aerodynamic contribution

a two–time–scale behavior, with fast dynamics for the pendulum motion and slow dynamics for the positioning task.

In order to properly address the design of novel rotorcraft configurations and the above–mentioned control strategies, a deep comprehension of the vehicle open–loop and closed–loop dynamics is required [14]. In the present work, a completely analytical framework is thus developed with the aim to describe the effects of suspended load oscillations on the dynamics of a multirotor, defined by 1) a rigid–body configuration and 2) an electric propulsion system made of a battery pack, electronic speed regulators, three–phase brushless motors, and fixed–pitch propellers. As a first step, it is assumed that the unloaded vehicle is characterized by a closed–loop behavior with known dynamic properties, which can be either obtained by a native control system (in the case of a commercial–off–the–shelf platform) or by the deployment of custom control laws, specifically designed for the particular application (in the case of an open source platform). In both cases, information about closed–loop dynamic properties can be indeed estimated by means of simple identification techniques [15]. In the latter case only, a dedicate analysis can be alternatively performed with the aim to relate selected control gains to the desired behavior, based on the exact knowledge of controller structure. To this end, an analytical framework is provided that allows to exactly determine the control gains of a sample PID controller as a function of desired closed–loop dynamic modes. In particular, an attitude control system is developed for roll and pitch angles stabilization, while speed regulators are designed to control the yaw rate and the vertical speed (an inner–loop control strategy which is widespread in commercial solutions such as PX4 autopilots [16]). After the multirotor is equipped with the payload, the combined system is shown to be underactuated over the oscillatory dynamics while unstable modes may appear. In this respect, a novel outer–loop auxiliary controller is developed with the aim to drive the loaded system back to the original stability properties or to improved ones, with the additional stabilization of the oscillatory dynamics. The novelty of the approach is also found in the derivation of a set of closed–form equations that allow to exactly size the outer–loop control gains as a function of the desired closed–loop dynamic features and a reduced set of system parameters.

For the purpose of the present analysis, the cable is assumed to be elastic and the suspension point is located in a distinct position with respect to the vehicle center of gravity, with the result that a coupling effect is produced between load oscillation and attitude motion. In this respect, the vertical displacement of the suspension point H can be considered as a design variable. In order to stabilize load oscillations according to the given requirements, the measurement of load position and velocity with respect to the hook point is needed. To this end, a recursive algorithm can be adopted to autonomously measure the swing angle and rate by means of the data available from the multirotor Inertial Measurement Unit (IMU), without the need to rely on extra sensors. Provided the multicopter is subject to known control inputs, data–fusion is performed through a Fading Gaussian Deterministic approach, whose theoretical background was recently investigated by some of the authors [17–19].

In what follows, reference frames and system dynamic equations are derived in Section 2. The definition of the companion/auxiliary controller is given in Section 3, where the analytical framework allowing the sizing of control gains is also outlined. The approach is numerically validated in Section 4, where multirotor description is detailed in terms of electric propulsion system components and Blade Element characterization of propellers [20]. The results of an experimental campaign are provided with the aim to describe the considered powerplant, showing the application of the gain–sizing technique to a nonlinear test case. A section of concluding remarks ends this paper.

The procedure developed in the present work has the merit of relative simplicity and the application of the proposed method proves to be encouraging in all those cases where the flying qualities of the lifting vehicle and the accuracy of the load positioning task both represent a fundamental requirement. Although the final equations of the auxiliary controller are derived for the particular case of an electric hexarotor, the philosophy has general validity and can be extended to both conventional and innovative rotorcraft configurations.

2. System modeling

Starting from the definition of reference frames, a 6 degrees–of–freedom mathematical model is adopted to describe the rotorcraft, with general expressions for the kinematics and dynamics of a rigid body with center of gravity CG.

2.1. Reference frames

Three right–handed orthogonal reference frames are introduced, according to the definitions in [20]:

1. an Earth-fixed North-East-Down frame, $\mathcal{F}_E = \{O_E; \boldsymbol{x}_E, \boldsymbol{y}_E, \boldsymbol{z}_E\}$: the origin, O_E, is arbitrarily fixed to a point on the Earth's surface, $\boldsymbol{x}_E$ aims in the direction of the geodetic North, $\boldsymbol{z}_E$ points downward along the Earth ellipsoid normal, and $\boldsymbol{y}_E$ completes a right-handed triad. This frame is assumed to be inertial under the assumption of flat and non–rotating Earth;
2. a Body–fixed frame, $\mathcal{F}_B = \{CG; \boldsymbol{x}_B, \boldsymbol{y}_B, \boldsymbol{z}_B\}$: the longitudinal axis $\boldsymbol{x}_B$ is positive out the nose of the rotorcraft in its selected plane of symmetry, being parallel to the plane containing the rotor hubs. $\boldsymbol{z}_B$ aims in the direction of the local vertical when the vehicle is at hover, pointing downwards, and $\boldsymbol{y}_B$ completes a right–handed triad;
3. a rotorcraft structural reference frame, $\mathcal{F}_S = \{O_S; \boldsymbol{x}_S, \boldsymbol{y}_S, \boldsymbol{z}_S\}$, used to locate CG and all vehicle components: the axes are parallel to the body–fixed frame axes, such that $\boldsymbol{x}_S = -\boldsymbol{x}_B$, $\boldsymbol{y}_S = \boldsymbol{y}_B$, and $\boldsymbol{z}_S = -\boldsymbol{z}_B$. The origin is located at some arbitrary point within the rotorcraft plane of symmetry. Stations (ST) are measured positive aft along the longitudinal axis. Buttlines (BL) are lateral distances, positive to the right, and waterlines (WL) are measured vertically, positive upward. A sketch of the rotorcraft including the selected $\mathcal{F}_S$ frame is reported in Figs. 1 and 2.

Let $s(\cdot) = \sin(\cdot)$ and $c(\cdot) = \cos(\cdot)$. Vector transformation between $\mathcal{F}_E$ and $\mathcal{F}_B$ is provided by the rotation matrix [19]

$$\boldsymbol{T}_{BE}(\boldsymbol{\alpha}) = \begin{bmatrix} c\theta\, c\psi & c\theta\, s\psi & -s\theta \\ s\phi\, s\theta\, c\psi - c\phi\, s\psi & s\phi\, s\theta\, s\psi + c\phi\, c\psi & s\phi\, c\theta \\ c\phi\, s\theta\, c\psi + s\phi\, s\psi & c\phi\, s\theta\, s\psi - s\phi\, c\psi & c\phi\, c\theta \end{bmatrix} \quad (1)$$

obtained by a 3-2-1 Euler rotation sequence where $\boldsymbol{\alpha} = [\phi, \theta, \psi]^T$ describes the attitude of the rotorcraft in terms of classical 'roll', 'pitch', and 'yaw' angles, respectively. The following notation is adopted: if $\boldsymbol{w}$ is an arbitrary vector, its components are transformed from $\mathcal{F}_E$ to $\mathcal{F}_B$ through $\boldsymbol{w}_B = \boldsymbol{T}_{BE}\, \boldsymbol{w}_E$. In what follows, the subscript B will be dropped for simplicity. In addition to the reference frames introduced above, a fourth useful definition is provided for a particular Local–Vertical Local–Horizontal frame, $\mathcal{F}_H = \{CG; \boldsymbol{x}_H, \boldsymbol{y}_H, \boldsymbol{z}_H\}$, with origin in CG. Vector transformation between $\mathcal{F}_E$ and $\mathcal{F}_H$ is provided by rotation matrix $\boldsymbol{T}_{HE} = \boldsymbol{T}_{BE}(\boldsymbol{\alpha}_0)$, where $\boldsymbol{\alpha}_0 = [0, 0, \psi]^T$ is determined by an elementary rotation about $\boldsymbol{z}_E$ with amplitude ψ. Although the definition of $\mathcal{F}_H$ does not provide additional information to attitude

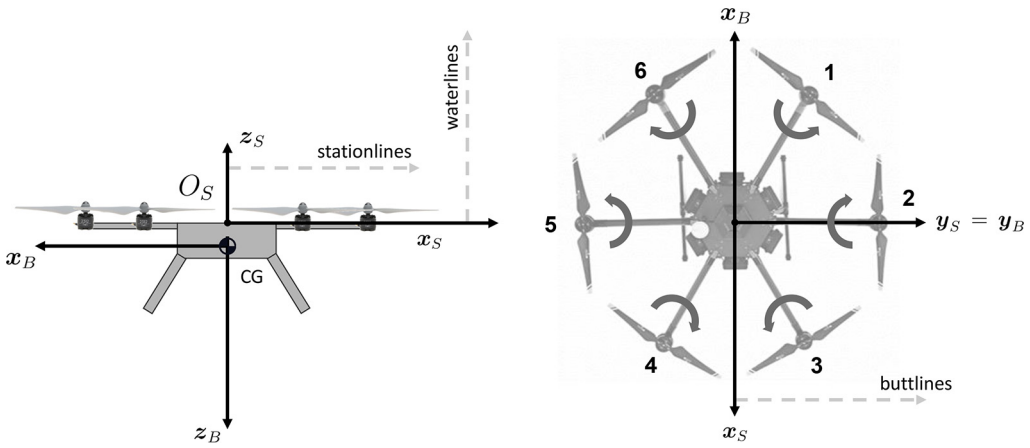

Fig. 1. Multirotor configuration and selected structural reference frame.

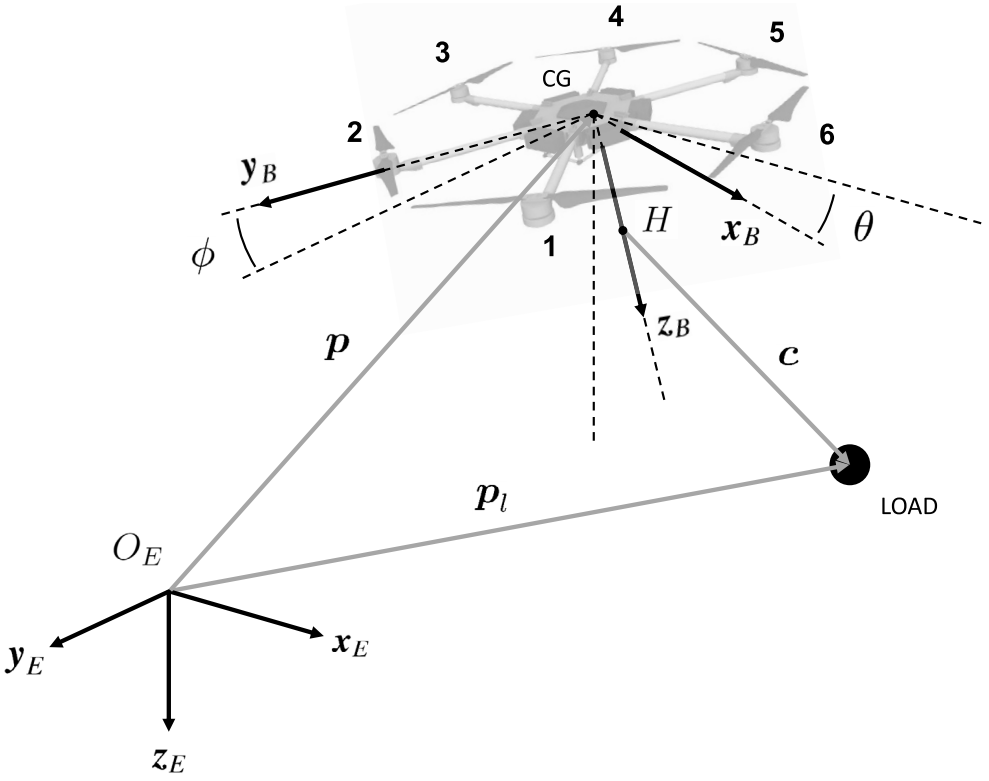

Fig. 2. Sketch of the rotorcraft slung–load system.

characterization, which is defined by $\boldsymbol{T}_{BE}$, it will be useful in Section 3 for the outline of auxiliary controller.

2.2. Multirotor dynamics

Multirotor dynamics is described by Newton–Euler equations of motion projected in $\mathcal{F}_B$, namely:

$$\dot{\boldsymbol{v}} = -\boldsymbol{\omega} \times \boldsymbol{v} + \boldsymbol{F}/m \tag{2}$$

$$\dot{\boldsymbol{\omega}} = \boldsymbol{J}^{-1}\left[-\boldsymbol{\omega} \times (\boldsymbol{J}\,\boldsymbol{\omega}) + \boldsymbol{M}\right] \tag{3}$$

where $\boldsymbol{v} = [u,\ v,\ w]^T$ is the linear velocity, $\boldsymbol{\omega} = [p,\ q,\ r]^T$ is the angular rate vector, $\boldsymbol{J} = diag\,(J_1,\ J_2,\ J_3)$ is the inertia tensor about CG with respect to $\mathcal{F}_B$, and m is the total mass of the rotorcraft. $\boldsymbol{F} = [F_1,\ F_2,\ F_3]^T$ and $\boldsymbol{M} = [M_1,\ M_2,\ M_3]^T$ are, respectively, the external force and moment vectors.

Rotorcraft attitude kinematics, which relates the generalized velocity $\dot{\boldsymbol{\alpha}}$ to the angular velocity $\boldsymbol{\omega}$, is given by [19]:

$$\dot{\boldsymbol{\alpha}} = \begin{bmatrix} 1 & \sin\phi\tan\theta & \cos\phi\tan\theta \\ 0 & \cos\phi & -\sin\phi \\ 0 & \sin\phi/\cos\theta & \cos\phi/\cos\theta \end{bmatrix} \boldsymbol{\omega} \tag{4}$$

while the position of the vehicle, $\boldsymbol{p}_E = [x_E,\ y_E,\ z_E]^T$, with components expressed in the inertial frame $\mathcal{F}_E$, is obtained from the equation:

$$\dot{\boldsymbol{p}}_E = \boldsymbol{T}_{BE}(\boldsymbol{\alpha})^T \boldsymbol{v} \tag{5}$$

The external force and moment vectors are made of gravity, aerodynamic, and cable contributions, namely $\boldsymbol{F} = \boldsymbol{F}^{(g)} + \boldsymbol{F}^{(a)} + \boldsymbol{T}_{BE}\,\boldsymbol{F}_E^{(c)}$ and $\boldsymbol{M} = \boldsymbol{M}^{(a)} + \boldsymbol{M}^{(c)}$. Taking into account Eq. (1), the gravity force vector expressed in the body frame is

$$\boldsymbol{F}^{(g)} = \boldsymbol{T}_{BE}(\boldsymbol{\alpha}) \begin{bmatrix} 0 \\ 0 \\ m\,g \end{bmatrix} = m\,g \begin{bmatrix} -\sin\theta \\ \sin\phi\,\cos\theta \\ \cos\phi\,\cos\theta \end{bmatrix} \tag{6}$$

where g is the gravitational acceleration, described by WGS84 Taylor series model [21]. The aerodynamic forces and moments are generated by the airframe and the set of propellers, namely $\boldsymbol{F}^{(a)} = \boldsymbol{F}^{(f)} + \boldsymbol{F}^{(r)}$ and $\boldsymbol{M}^{(a)} = \boldsymbol{M}^{(f)} + \boldsymbol{M}^{(r)}$. Airframe aerodynamics, limited to drag modeling, is assessed by the equivalent flat plate area model. The force vector, expressed in the body frame, is

$$\boldsymbol{F}^{(f)} = -\frac{1}{2}\rho \begin{bmatrix} A_1|u|u & A_2|v|v & A_3|w|w \end{bmatrix}^T \tag{7}$$

where A_1, A_2, and A_3 are the equivalent flat–plate drag areas facing the three body–frame axes and ρ is the air density. The moment generated by $\boldsymbol{F}^{(f)}$ is $\boldsymbol{M}^{(f)} = \boldsymbol{d}_{CP} \times \boldsymbol{F}^{(f)}$, where $\boldsymbol{d}_{CP} = [STA_{CG} - STA_{CP},\ BL_{CP} - BL_{CG},\ WL_{CG} - WL_{CP}]^T$ is the vector directed from CG to the center of pressure CP of the airframe, assumed to be a fixed point in the body–frame. The effect of rotor induced velocity on airframe drag is neglected [14].

Without loss of generality, a planar vehicle configuration with $N = 6$ equal rotors is considered where the thrust T_j, $j \in 1, \ldots, N$, generated by the j–th rotor is directed along $\boldsymbol{z}_B$, pointing upward. Generated forces and moments are obtained as

$$\boldsymbol{F}^{(r)} = \sum_{j=1}^{N} \boldsymbol{F}_j^{(r)}, \quad \boldsymbol{M}^{(r)} = \sum_{j=1}^{N} \boldsymbol{M}_j^{(r)} \tag{8}$$

provided the j–th rotor has number of blades n_b, radius R, area $A = \pi R^2$, mean aerodynamic chord $\bar{c}$, and position $\boldsymbol{d}_{R_j} = [STA_{CG} - STA_{R_j},\ BL_{R_j} - BL_{CG},\ WL_{CG} - WL_{R_j}]^T$, with components expressed in $\mathcal{F}_B$. Under the assumption of incompressible flow, the j–th rotor aerodynamics is described by Momentum Theory (MT) and Blade Element Theory (BET) according to the approach detailed in [20], whose nomenclature and mathematical models are adopted in the present framework. In particular, the following assumptions are made: a) rotor blades are rigid in bending and torsion with null hinge offset ratio, flapping spring constant, and pitch–flap coupling ratio; b) blade flow stall is disregarded; c) no inflow dynamics is modeled; d) the blades do not flap and the pre–cone angle, a_0, is treated as a preset constant.

Let Ω_j be the j–th rotor angular rate, such that $V_{tip\,j} = \Omega_j R$ is blade tip speed. Differently to some of the assumptions provided in [20], rotor blades are characterized by airfoils with lift–curve slope $a < 2\pi$ 1/rad and profile drag coefficient, averaged along the blade, estimated as [22]:

$$C_{d\,j} = 0.1166\,\mathrm{Re}_j^{-0.2} + 0.3\left(\frac{6\,C_{T\,j}}{\sigma\,a}\right)^2 \tag{9}$$

The first term in Eq. (9) accounts for the blade parasitic drag, where $\mathrm{Re}_j = \rho\,c_{75}\,V_{75\,j}/\mu$ is the Reynolds number at 75% blade radius [23], c_{75} and $V_{75\,j} \approx \sqrt{v_{i\,j}^2 + \left(0.75 \cdot V_{tip\,j}\right)^2}$ respectively represent the local airfoil chord and the relative airspeed, $v_{i\,j}$ is the induced speed at the j–th rotor disc, and μ is the dynamic viscosity of the air. The second term in Eq. (9) accounts for blade induced drag as a function of thrust coefficient, $C_{T\,j} = T_j/(\rho\,A\,V_{tip\,j}^2)$, and rotor solidity, $\sigma = n_b\,\bar{c}/(\pi\,R)$. With respect to the characterization of rotors inflow, a number of non–ideal effects, including tip losses, nonuniform inflow, wake swirl and contraction, and blades interference are accounted for by an induced power factor $k_{ind} > 1$, assumed to be a constant. Rotors in–ground effect for very–low gear configurations is provided by the model in [24] and the inflow iterative scheme is solved according to Halley's method with damping coefficient equal to 0.01 [25]. Air parameters are calculated from the International Standard Atmosphere (ISA) model as a function of rotorcraft altitude [26].

Control of the j–th rotor speed is performed by commanding the value δ_j of the signal to the j–th motor driver. In particular, Ω_j is assumed to be a function of throttle signal δ_j, namely

$$\Omega_j = k_\Omega\,\delta_j^n \tag{10}$$

where $k_\Omega > 0$ and $0 < n < 1$ are experimental coefficients. In the case when, for example, Pulse Width Modulation (PWM) technology is adopted, $\delta_j = PWM_j - PWM_{idle}$ is the command increment with respect to the idle condition $PWM_j = PWM_{idle}$, for which $\Omega_j = 0$. Control signals are generated by the onboard computer according to the following motor–mixing scheme:

$$\delta_1 = -\delta_{roll} + \delta_{pitch} + \delta_{yaw} + \delta_v + \delta_{fwd} \tag{11}$$

$$\delta_2 = -2\,\delta_{roll} - \delta_{yaw} + \delta_v + \delta_{fwd} \tag{12}$$

$$\delta_3 = -\delta_{roll} - \delta_{pitch} + \delta_{yaw} + \delta_v + \delta_{fwd} \tag{13}$$

$$\delta_4 = \delta_{roll} - \delta_{pitch} - \delta_{yaw} + \delta_v + \delta_{fwd} \tag{14}$$

$$\delta_5 = 2\,\delta_{roll} + \delta_{yaw} + \delta_v + \delta_{fwd} \tag{15}$$

$$\delta_6 = \delta_{roll} + \delta_{pitch} - \delta_{yaw} + \delta_v + \delta_{fwd} \tag{16}$$

which is based on the particular configuration depicted in Fig. 2. The doubling of δ_{roll} contribution on motors 2 and 5 is adopted to avoid unbalanced yawing moments induced by roll attitude corrections. The signals δ_{roll}, δ_{pitch}, and δ_{yaw} are the outputs of 3 different controllers respectively aiming at the stabilization of roll, pitch, and yaw dynamics. The contribution related to δ_v is used to regulate the speed of the multirotor along the Earth–fixed vertical axis. Finally, the additive term δ_{fwd} is a feed–forward throttle signal adopted for rapid trimming purposes and is typically tuned to allow a near–hover condition with 50% throttle command (for example in a RC device), thus providing sufficient maneuvering margin along the vertical axis. Disregarding the particular rotor configuration, the proposed control strategy is representative of many applications where the multirotor is piloted through high–level commands in terms of desired attitude and climb speed (inner–loop stabilization [16]). Such commands are, in turn, generated by the pilot or by a dedicated guidance and navigation loop to perform trajectory or waypoint tracking, with major use of positioning systems and obstacle detection devices [27].

2.3. Suspended load dynamics

The load is assumed to be a point with mass m_c, connected by a cable to the multirotor at the hook point H with coordinates $\boldsymbol{h} = [STA_{CG} - STA_H,\ BL_H - BL_{CG},\ WL_{CG} - WL_H]^T = [h_1,\ h_2,\ h_3]^T$ in $\mathcal{F}_B$. Payload dynamics is described by Newton–Euler equations projected in $\mathcal{F}_E$, namely:

$$m_c\,\dot{\boldsymbol{v}}_{cE} = \boldsymbol{F}_{cE} = \begin{bmatrix} 0 \\ 0 \\ m_c\,g \end{bmatrix} + \boldsymbol{F}_{c_E}^{(d)} + \boldsymbol{F}_{c_E}^{(c)} \tag{17}$$

where $\boldsymbol{F}_{c_E}^{(c)} = -\boldsymbol{F}_E^{(c)}$ is the force exerted by the multirotor on the load through an elastic cable with Hooke's constant $K > 0$ and nominal length L. $\boldsymbol{F}_{c_E}^{(d)}$ is the aerodynamic force acting on the payload, here calculated as

$$\boldsymbol{F}_{c_E}^{(d)} = -\frac{1}{2}\,\rho\,A_c\,C_{dc}\,\|\boldsymbol{v}_{cE}\|\,\boldsymbol{v}_{cE} \tag{18}$$

where C_{dc} is the payload drag coefficient and A_c is a reference area for drag computation. The cable is assumed to be mass–less and

its aerodynamic drag is disregarded. Provided $\boldsymbol{p}_{cE}$ is the position of the load, obtained from

$$\dot{\boldsymbol{p}}_{cE} = \boldsymbol{v}_{cE}, \tag{19}$$

the vector describing the actual orientation and length of the cable in $\mathcal{F}_E$ is $\boldsymbol{c}_E = \boldsymbol{p}_{cE} - \boldsymbol{p}_E - \boldsymbol{T}_{BE}^T \boldsymbol{h}$. According to Hookes' model, the force $\boldsymbol{F}_E^{(c)}$ results from the linear–elastic equation

$$\boldsymbol{F}_E^{(c)} = K\,\Delta L\,\hat{\boldsymbol{c}}_E \tag{20}$$

where $\Delta L = \|\boldsymbol{c}_E\| - L$ is the elastic deformation and $\hat{\boldsymbol{c}}_E = \boldsymbol{c}_E / \|\boldsymbol{c}_E\|$ is the unit vector directed along the cable. The moment generated by force $\boldsymbol{F}_E^{(c)}$ on the multirotor, expressed in $\mathcal{F}_B$, is $\boldsymbol{M}^{(c)} = \boldsymbol{h} \times \left[\boldsymbol{T}_{BE}\,\boldsymbol{F}_E^{(c)}\right]$.

3. Closed–loop system stabilization

In what follows the system described in Section 2 is linearized about the hovering condition in both the unloaded and the loaded configuration. In the latter case, an auxiliary controller is designed to stabilize the underactuated system with almost–desired dynamics. To this end, some preliminary assumptions are made:

Assumption 1. Rotor forces and moments are generated only by thrust and torque contributions respectively calculated as

$$T_j = k_T\,\Omega_j^2, \quad Q_j = k_Q\,\Omega_j^2 \tag{21}$$

with $k_T = \chi\,\bar{k}_T$ and $k_Q = \chi\,\bar{k}_Q$. $\bar{k}_T$ and $\bar{k}_Q$ are positive constants determined experimentally at air density ρ_{exp} while $\chi = \rho/\rho_{exp}$ is a density scaling parameter.

Assumption 2. The aerodynamics of the airframe and of the suspended load is disregarded.

Assumption 3. The suspension point has coordinates $h_1 = h_2 = 0$ and $h_3 \neq 0$ in $\mathcal{F}_B$, which occurs when $STA_H = STA_{CG}$, $BL_H = BL_{CG}$, and $WL_H \neq WL_{CG}$. In addition, a balanced configuration with $STA_{CG} = BL_{CG} = 0$ is considered.

3.1. Unloaded configuration

Let $e_\phi = \phi_d - \phi$, $e_\theta = \theta_d - \theta$, $e_r = r_d - r$, and $e_v = \dot{z}_{E_d} - \dot{z}_E$ be error vectors respectively calculated from the desired values of roll and pitch angles, yaw rate, and Earth–fixed vertical speed. A set of inner–loop control signals $\delta_v = \delta_v^{(inn)}(e_v,\,\varepsilon_v)$, $\delta_{yaw} = \delta_{yaw}^{(inn)}(e_r,\,\varepsilon_r)$, $\delta_{roll} = \delta_{roll}^{(inn)}(e_\phi,\,\varepsilon_\phi)$, and $\delta_{pitch} = \delta_{pitch}^{(inn)}(e_\theta,\,\varepsilon_\theta)$ is assumed to stabilize the origin of the error system described by state vector $\boldsymbol{x} \in \mathbb{R}^{10}$:

$$\boldsymbol{x} = \left[e_v,\,\varepsilon_v,\,e_r,\,\varepsilon_r,\,p,\,e_\phi,\,\varepsilon_\phi,\,q,\,e_\theta,\,\varepsilon_\theta\right]^T \tag{22}$$

where

$$\dot{\varepsilon}_v = e_v, \quad \dot{\varepsilon}_r = e_r, \quad \dot{\varepsilon}_\phi = e_\phi, \quad \dot{\varepsilon}_\theta = e_\theta \tag{23}$$

The stability of the error system is evaluated by linearization about the hovering condition, where $T_j = m\,g/6$ and the feed–forward contribution to each motor results to be

$$\delta_{fwd} = \left(\frac{m\,g}{6\,k_T\,k_\Omega^2}\right)^{\frac{1}{2n}} \tag{24}$$

By imposing $\dot{z}_{E_d} = 0$, $r_d = 0$, and $\phi_d = \theta_d = 0$, the standard linear form $\dot{\boldsymbol{x}} = \boldsymbol{A}\,\boldsymbol{x}$ is obtained with $\boldsymbol{A} \in \mathbb{R}^{10\times 10}$. The following assumption is made on the dynamic properties of $\boldsymbol{A}$.

Assumption 4. The inner–loop control system is designed and tuned such that the state matrix $\boldsymbol{A}$ is block diagonal, namely:

$$\boldsymbol{A} = \begin{bmatrix} \boldsymbol{A}_v & 0 & \cdots & 0 \\ 0 & \boldsymbol{A}_{yaw} & \cdots & 0 \\ \vdots & \vdots & \boldsymbol{A}_{roll} & 0 \\ 0 & 0 & \cdots & \boldsymbol{A}_{pitch} \end{bmatrix} \tag{25}$$

Each decoupled subsystem, respectively represented by

$$\boldsymbol{A}_v\,(\lambda_{v1},\,\lambda_{v2}) \in \mathbb{R}^{2\times 2}, \quad \boldsymbol{A}_{yaw}\left(\lambda_{yaw_1},\,\lambda_{yaw_2}\right) \in \mathbb{R}^{2\times 2},$$
$$\boldsymbol{A}_{roll}\,(\lambda_{roll_1},\,\lambda_{roll_2},\,\lambda_{roll_3}) \in \mathbb{R}^{3\times 3},$$

and

$$\boldsymbol{A}_{pitch}\left(\lambda_{pitch_1},\,\lambda_{pitch_2},\,\lambda_{pitch_3}\right) \in \mathbb{R}^{3\times 3}$$

is characterized by a set of prescribed stable eigenvalues λ_{v1}, λ_{v2}, λ_{yaw_1}, λ_{yaw_2}, λ_{roll1}, λ_{roll2}, λ_{roll3}, λ_{pitch_1}, λ_{pitch_2}, and λ_{pitch_3}.

Remark 1. Different control strategies can be adopted to comply with Assumption 4. In what follows, sample regulators are proposed which are based on proportional–integral–derivative approach:

$$\delta_v = k_{p_v}\,e_v + k_{iv}\,\varepsilon_v \tag{26}$$
$$\delta_{yaw} = k_{p_r}\,e_r + k_{ir}\,\varepsilon_r \tag{27}$$
$$\delta_{roll} = k_{p_\phi}\,e_\phi + k_{i\phi}\,\varepsilon_\phi + k_p\,p \tag{28}$$
$$\delta_{pitch} = k_{p_\theta}\,e_\theta + k_{i\theta}\,\varepsilon_\theta + k_q\,q \tag{29}$$

Let $\Delta = 4k_\Omega^2\,n\,\delta_{fwd}^{2n-1}$. It is straightforward to prove that 1) matrix $\boldsymbol{A}$ is block diagonal and 2) subsystems state matrices are, respectively:

$$\boldsymbol{A}_v = \begin{bmatrix} \frac{3k_T\,\Delta}{m} k_{p_v} & \frac{3k_T\,\Delta}{m} k_{iv} \\ 1 & 0 \end{bmatrix}, \tag{30}$$

$$\boldsymbol{A}_{yaw} = \begin{bmatrix} -\frac{3k_Q\,\Delta}{J_3} k_{p_r} & -\frac{3k_Q\,\Delta}{J_3} k_{ir} \\ 1 & 0 \end{bmatrix}, \tag{31}$$

$$\boldsymbol{A}_{roll} = \begin{bmatrix} \frac{3bk_T\,\Delta}{J_1} k_p & \frac{3bk_T\,\Delta}{J_1} k_{p_\phi} & \frac{3bk_T\,\Delta}{J_1} k_{i\phi} \\ -1 & 0 & 0 \\ 0 & 1 & 0 \end{bmatrix}, \tag{32}$$

and

$$\boldsymbol{A}_{pitch} = \begin{bmatrix} \frac{\sqrt{3}bk_T\,\Delta}{J_2} k_q & \frac{\sqrt{3}bk_T\,\Delta}{J_2} k_{p_\theta} & \frac{\sqrt{3}bk_T\,\Delta}{J_2} k_{i\theta} \\ -1 & 0 & 0 \\ 0 & 1 & 0 \end{bmatrix} \tag{33}$$

where $b = \sqrt{STA_{R_j}^2 + BL_{R_j}^2}$ is rotor arm length on the plane $\boldsymbol{x}_S$–$\boldsymbol{y}_S$. Control gains required for correct pole placement to each subsystem result to be, according to Assumption 4,

$$k_{iv} = -\frac{\Pi_v\,\delta_{fwd}}{2\,g\,n}, \quad k_{p_v} = \frac{\Sigma_v\,\delta_{fwd}}{2\,g\,n}, \tag{34}$$

$$k_{ir} = \frac{J_3\,\Pi_{yaw}\,k_T\,\delta_{fwd}}{2\,m\,g\,n\,k_Q}, \tag{35}$$

$$k_{p_r} = -\frac{J_3\,\Sigma_{yaw}\,k_T\,\delta_{fwd}}{2\,m\,g\,n\,k_Q} \tag{36}$$

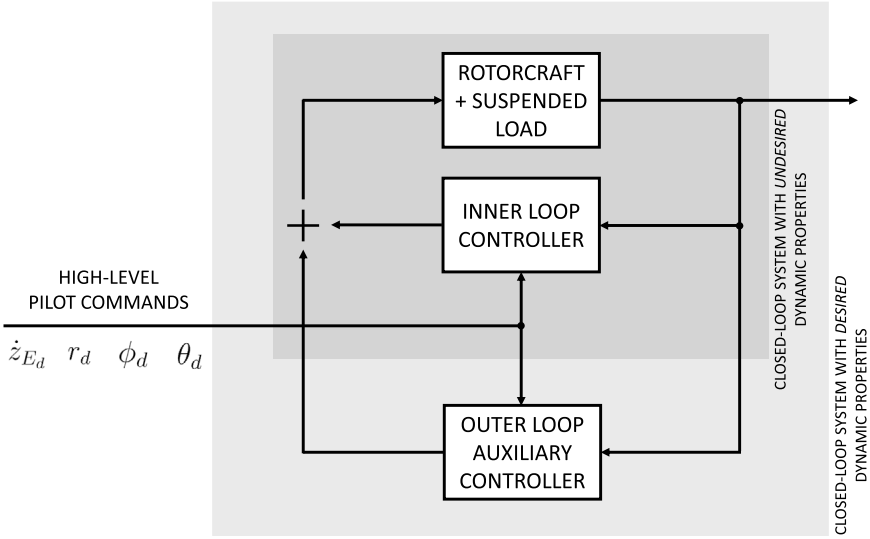

Fig. 3. The control strategy proposed for the stabilization of multirotor slung–load system.

$$k_{i\phi} = -\frac{J_1\,\Pi_{roll}\,\delta_{fwd}}{2\,b\,m\,g\,n}, \quad k_{p_\phi} = \frac{J_1\,\Xi_{roll}\,\delta_{fwd}}{2\,b\,m\,g\,n}, \tag{37}$$

and

$$k_p = \frac{J_1\,\Sigma_{roll}\,\delta_{fwd}}{2\,b\,m\,g\,n} \tag{38}$$

where $\Sigma_v = \lambda_{v1} + \lambda_{v2}$, $\Pi_v = \lambda_{v1}\,\lambda_{v2}$, $\Sigma_{yaw} = \lambda_{yaw_1} + \lambda_{yaw_2}$, $\Pi_{yaw} = \lambda_{yaw_1}\,\lambda_{yaw_2}$, $\Sigma_{roll} = \lambda_{roll_1} + \lambda_{roll_2} + \lambda_{roll_3}$, $\Pi_{roll} = \lambda_{roll_1}\,\lambda_{roll_2}\,\lambda_{roll_3}$, and $\Xi_{roll} = \lambda_{roll_1}\,\lambda_{roll_2} + \lambda_{roll_3}\,(\lambda_{roll_1} + \lambda_{roll_2})$. In order to reasonably provide the multirotor with the same dynamic behavior about the roll and the pitch axes, namely $\lambda_{pitch_1} = \lambda_{roll_1}$, $\lambda_{pitch_2} = \lambda_{roll_2}$, and $\lambda_{pitch_3} = \lambda_{roll_3}$, the remaining control gains are scaled as follows:

$$k_{i\theta} = J_2/J_1\,\sqrt{3}\,k_{i\phi}, \quad k_{p_\theta} = J_2/J_1\,\sqrt{3}\,k_{p_\phi}, \tag{39}$$

$$k_q = J_2/J_1\,\sqrt{3}\,k_p \tag{40}$$

With the proposed control strategy, subsystem matrices in Eqs. (30)–(33) respectively become:

$$\boldsymbol{A}_v\,(\lambda_{v1},\,\lambda_{v2}) = \begin{bmatrix} \Sigma_v & -\Pi_v \\ 1 & 0 \end{bmatrix}, \tag{41}$$

$$\boldsymbol{A}_{yaw}\,(\lambda_{yaw_1},\,\lambda_{yaw_2}) = \begin{bmatrix} \Sigma_{yaw} & -\Pi_{yaw} \\ 1 & 0 \end{bmatrix}, \tag{42}$$

$$\boldsymbol{A}_{roll}\,(\lambda_{roll1},\,\lambda_{roll2},\,\lambda_{roll3}) = \begin{bmatrix} \Sigma_{roll} & \Xi_{roll} & -\Pi_{roll} \\ -1 & 0 & 0 \\ 0 & 1 & 0 \end{bmatrix}, \tag{43}$$

while $\boldsymbol{A}_{pitch} = \boldsymbol{A}_{roll}$.

3.2. Loaded configuration with active swing–control

Consider the isolated multirotor platform described above under Assumptions 1–3. In the presence of a suspended load, the hovering condition is obtained by generating $T_j = (m + m_c)\,g/6$ through the throttle signal:

$$\bar{\delta}_{fwd} = \left[\frac{(m + m_c)\,g}{6\,k_T\,k_\Omega^2}\right]^{\frac{1}{2n}} \tag{44}$$

The cable equilibrium condition is described by the desired vector $\boldsymbol{c}_{Ed} = [0,\,0,\,L_d]^T$, where $L_d = L + m_c\,g/K$ is the actual cable length. Let $\boldsymbol{\eta}_E = \boldsymbol{c}_{Ed} - \boldsymbol{c}_E = [\eta_{1E},\,\eta_{2E},\,\eta_{3E}]^T$ be the error, expressed in $\mathcal{F}_E$, between the desired and the actual load position relative to the suspension point. The dynamics of the cable error vector is expressed as

$$\dot{\boldsymbol{\eta}}_E = \boldsymbol{v}_E \tag{45}$$

where $\boldsymbol{v}_E = [v_{1E},\,v_{2E},\,v_{3E}]^T$ follows from

$$\begin{aligned} \dot{\boldsymbol{v}}_E = {} & \boldsymbol{T}_{BE}^T\,\boldsymbol{F}/m - \boldsymbol{F}_{cE}/m_c \\ & + \boldsymbol{T}_{BE}^T\,[\dot{\boldsymbol{\omega}} \times \boldsymbol{h} + \boldsymbol{\omega} \times (\boldsymbol{\omega} \times \boldsymbol{h})] \end{aligned} \tag{46}$$

and $\boldsymbol{v}_E = -\dot{\boldsymbol{c}}_E$.

Consider the system described by the extended state vector $\bar{\boldsymbol{x}} \in \mathbb{R}^{16}$:

$$\begin{aligned} \bar{\boldsymbol{x}} = \big[& e_v,\,\varepsilon_v,\,v_{3E},\,\eta_{3E},\,e_r,\,\varepsilon_r,\,p,\,e_\phi,\,\varepsilon_\phi, \\ & v_{2E},\,\eta_{2E},\,q,\,e_\theta,\,\varepsilon_\theta,\,v_{1E},\,\eta_{1E}\big]^T \end{aligned} \tag{47}$$

Let $\boldsymbol{\eta}_H = [\eta_{1H},\,\eta_{2H},\,\eta_{3H}]^T$ be the load–displacement error vector, expressed in $\mathcal{F}_H$, obtained as $\boldsymbol{\eta}_H = \boldsymbol{T}_{HE}\,\boldsymbol{\eta}_E$, with $\boldsymbol{T}_{HE}$ defined in Section 2.1. Also, let $\boldsymbol{v}_H = \boldsymbol{T}_{HE}\,\boldsymbol{v}_E$.

Assume that the control signals in Eqs. (11)–(16) are expressed as the sum of 2 contributions, namely $\delta_v = \delta_v^{(inn)} + \delta_v^{(aux)}$, $\delta_{yaw} = \delta_{yaw}^{(inn)} + \delta_{yaw}^{(aux)}$, $\delta_{roll} = \delta_{roll}^{(inn)} + \delta_{roll}^{(aux)}$, and $\delta_{pitch} = \delta_{pitch}^{(inn)} + \delta_{pitch}^{(aux)}$, where $\delta_v^{(inn)}$, $\delta_{yaw}^{(inn)}$, $\delta_{roll}^{(inn)}$, and $\delta_{pitch}^{(inn)}$ are inner–loop contributions designed under Assumption 4. The terms $\delta_v^{(aux)}$, $\delta_{yaw}^{(aux)}$, $\delta_{roll}^{(aux)}$, and $\delta_{pitch}^{(aux)}$ are a set of auxiliary controllers in the form:

$$\delta_v^{(aux)} = \bar{k}_{p_v}\,e_v + \bar{k}_{i\,v}\,\varepsilon_v \tag{48}$$

$$\delta_{yaw}^{(aux)} = \bar{k}_{p_r}\,e_r + \bar{k}_{ir}\,\varepsilon_r \tag{49}$$

$$\begin{aligned} \delta_{roll}^{(aux)} = {} & \bar{k}_{p_\phi}\,e_\phi + \bar{k}_{i\phi}\,\varepsilon_\phi + \bar{k}_p\,p \\ & + \bar{k}_{\eta_2}\,\eta_{2H} + \bar{k}_{v_2}\,v_{2H} \end{aligned} \tag{50}$$

$$\begin{aligned} \delta_{pitch}^{(aux)} = {} & \bar{k}_{p_\theta}\,e_\theta + \bar{k}_{i\theta}\,\varepsilon_\theta + \bar{k}_q\,q \\ & + \bar{k}_{\eta_1}\,\eta_{1H} + \bar{k}_{v_1}\,v_{1H} \end{aligned} \tag{51}$$

The following results provide the values of control gains that allow the regulators in Eqs. (48)–(51) to stabilize the origin of the extended–state system in Eq. (47) with desired dynamic behavior, according to the scheme depicted in Fig. 3.

Theorem 1. *Consider the dynamic system identified by the extended state in Eq. (47) under Assumptions 1–3. Assume that a set of controllers* $\delta_v^{(inn)}$, $\delta_{yaw}^{(inn)}$, $\delta_{roll}^{(inn)}$, *and* $\delta_{pitch}^{(inn)}$ *is designed under Assumption 4 and is supported by the auxiliary controllers in Eqs. (48)–(51). Then, the linearized extended system, described by state–matrix* $\bar{\boldsymbol{A}} \in \mathbb{R}^{16\times 16}$, *assumes the block–diagonal form:*

$$\bar{\boldsymbol{A}} = \begin{bmatrix} \bar{\boldsymbol{A}}_v & 0 & \cdots & 0 \\ 0 & \bar{\boldsymbol{A}}_{yaw} & \dots & 0 \\ \vdots & \vdots & \bar{\boldsymbol{A}}_{roll} & 0 \\ 0 & 0 & \dots & \bar{\boldsymbol{A}}_{pitch} \end{bmatrix} \tag{52}$$

The decoupled subsystems

$$\bar{\boldsymbol{A}}_{yaw}\left(\bar{\lambda}_{yaw_1}, \bar{\lambda}_{yaw_2}\right) \in \mathbb{R}^{2\times 2}, \tag{53}$$

$$\bar{\boldsymbol{A}}_{roll}\left(\bar{\lambda}_{roll_1}, \bar{\lambda}_{roll_2}, \bar{\lambda}_{roll_3}, \bar{\lambda}_{roll_4}, \bar{\lambda}_{roll_5}\right) \in \mathbb{R}^{5\times 5}, \tag{54}$$

and

$$\bar{\boldsymbol{A}}_{pitch}\left(\bar{\lambda}_{pitch_1}, \bar{\lambda}_{pitch_2}, \bar{\lambda}_{pitch_3}, \bar{\lambda}_{pitch_4}, \bar{\lambda}_{pitch_5}\right) \in \mathbb{R}^{5\times 5} \tag{55}$$

are respectively characterized by a set of prescribed stable eigenvalues

$$\bar{\lambda}_{yaw_1}, \bar{\lambda}_{yaw_2}, \tag{56}$$

$$\bar{\lambda}_{roll_1}, \bar{\lambda}_{roll_2}, \bar{\lambda}_{roll_3}, \bar{\lambda}_{roll_4}, \bar{\lambda}_{roll_5}, \tag{57}$$

and

$$\bar{\lambda}_{pitch_1}, \bar{\lambda}_{pitch_2}, \bar{\lambda}_{pitch_3}, \bar{\lambda}_{pitch_4}, \bar{\lambda}_{pitch_5} \tag{58}$$

such that $\bar{\lambda}_{pitch_1} = \bar{\lambda}_{roll_1}$, $\bar{\lambda}_{pitch_2} = \bar{\lambda}_{roll_2}$, $\bar{\lambda}_{pitch_3} = \bar{\lambda}_{roll_3}$, $\bar{\lambda}_{pitch_4} = \bar{\lambda}_{roll_4}$, $\bar{\lambda}_{pitch_5} = \bar{\lambda}_{roll_5}$ *if auxiliary control gains are selected as follows:*

$$\bar{k}_{i_r} = \frac{J_3\, k_T\, \bar{\delta}_{fwd}}{2\, k_Q\, (m+m_c)\, g\, n}\left(\bar{\Pi}_{yaw} - \Gamma\, \Pi_{yaw}\right) \tag{59}$$

$$\bar{k}_{p_r} = \frac{J_3\, k_T\, \bar{\delta}_{fwd}}{2\, k_Q\, (m+m_c)\, g\, n}\left(\Gamma\, \Sigma_{yaw} - \bar{\Sigma}_{yaw}\right) \tag{60}$$

$$\bar{k}_{\eta_2} = \frac{1}{L_d + h_3}\left\{-\Lambda\, G_1 + \frac{J_1\, \bar{\delta}_{fwd}}{2\, b\, (m+m_c)\, g\, n} \cdot \left[G_3 - g\, \frac{J_1\,(m+m_c) + h_3\, m\, m_c\, (L_d+h_3)}{J_1\, L_d\, m}\right]\right\} \tag{61}$$

$$\bar{k}_{\nu_2} = \Lambda\left[\frac{m^2\, L_d^2\, G_0 - m\,(m+m_c)\, g\, L_d\, G_2 + (m+m_c)^2\, g^2\, G_4}{m\,(m+m_c)\, g\, L_d\,(L_d+h_3)}\right] \tag{62}$$

$$\bar{k}_{i_\phi} = \Lambda\, G_0 + \frac{J_1\, \Pi_{roll}\, \delta_{fwd}}{2\, b\, m\, g\, n} \tag{63}$$

$$\bar{k}_{p_\phi} = \Lambda\, G_1 - \frac{J_1\, \Xi_{roll}\, \delta_{fwd}}{2\, b\, m\, g\, n} + \bar{k}_{\eta_2}\, L_d \tag{64}$$

$$\bar{k}_p = -\frac{(m+m_c)\, g\, \Lambda\, G_4}{m\, L_d} - \frac{J_1\, \Sigma_{roll}\, \delta_{fwd}}{2\, b\, m\, g\, n} + \bar{k}_{\nu_2}\, h_3 \tag{65}$$

$$\bar{k}_{\eta_1} = -\frac{\sqrt{3}\, J_2/J_1}{L_d + h_3}\left\{-\Lambda\, G_1 + \frac{J_1\, \bar{\delta}_{fwd}}{2\, b\, (m+m_c)\, g\, n} \cdot \left[G_3 - g\, \frac{m + m_c + J_2\, h_3\, m\, m_c\, (L_d+h_3)}{L_d\, m}\right]\right\} \tag{66}$$

$$\bar{k}_{\nu_1} = -J_2/J_1\, \sqrt{3}\, \bar{k}_{\nu_2} \tag{67}$$

$$\bar{k}_{i_\theta} = J_2/J_1\, \sqrt{3}\, \bar{k}_{i_\phi}, \quad \bar{k}_q = J_2/J_1\, \sqrt{3}\, \bar{k}_p \tag{68}$$

$$\bar{k}_{p_\theta} = J_2/J_1\, \sqrt{3}\, \bar{k}_{p_\phi} - L_d\left(\bar{k}_{\eta_1} + J_2/J_1\, \sqrt{3}\, \bar{k}_{\eta_2}\right) \tag{69}$$

provided

$$\bar{\Pi}_{yaw} = \bar{\lambda}_{yaw_1}\, \bar{\lambda}_{yaw_2}, \quad \bar{\Sigma}_{yaw} = \bar{\lambda}_{yaw_1} + \bar{\lambda}_{yaw_2}, \tag{70}$$

$$\Gamma = \left(1 + \frac{m_c}{m}\right)^{1-\frac{1}{2n}}, \quad \Lambda = \frac{J_1\, L_d\, m\, \bar{\delta}_{fwd}}{2\, b\, n\, (m+m_c)^2\, g^2}, \tag{71}$$

and

$$\begin{aligned} G_0 &= -\bar{\lambda}_{roll_1}\, \bar{\lambda}_{roll_2}\, \bar{\lambda}_{roll_3}\, \bar{\lambda}_{roll_4}\, \bar{\lambda}_{roll_5} \\ G_1 &= \bar{\lambda}_{roll_5}\left\{\bar{\lambda}_{roll_4}\left[\bar{\lambda}_{roll_3}\left(\bar{\lambda}_{roll_1} + \bar{\lambda}_{roll_2}\right) + \bar{\lambda}_{roll_1}\, \bar{\lambda}_{roll_2}\right] + \bar{\lambda}_{roll_1}\, \bar{\lambda}_{roll_2}\, \bar{\lambda}_{roll_3}\right\} \\ &\quad + \bar{\lambda}_{roll_1}\, \bar{\lambda}_{roll_2}\, \bar{\lambda}_{roll_3}\, \bar{\lambda}_{roll_4} \\ G_2 &= -\bar{\lambda}_{roll_4}\left[\bar{\lambda}_{roll_3}\left(\bar{\lambda}_{roll_1} + \bar{\lambda}_{roll_2}\right) + \bar{\lambda}_{roll_1}\, \bar{\lambda}_{roll_2}\right] \\ &\quad - \bar{\lambda}_{roll_1}\, \bar{\lambda}_{roll_2}\, \bar{\lambda}_{roll_3} \\ &\quad - \bar{\lambda}_{roll_5}\left[\bar{\lambda}_{roll_3}\left(\bar{\lambda}_{roll_1} + \bar{\lambda}_{roll_2}\right) + \bar{\lambda}_{roll_1}\, \bar{\lambda}_{roll_2} \right. \\ &\quad \left. + \bar{\lambda}_{roll_4}\left(\bar{\lambda}_{roll_1} + \bar{\lambda}_{roll_2} + \bar{\lambda}_{roll_3}\right)\right] \\ G_3 &= \bar{\lambda}_{roll_3}\left(\bar{\lambda}_{roll_1} + \bar{\lambda}_{roll_2}\right) + \bar{\lambda}_{roll_1}\, \bar{\lambda}_{roll_2} \\ &\quad + \bar{\lambda}_{roll_4}\left(\bar{\lambda}_{roll_1} + \bar{\lambda}_{roll_2} + \bar{\lambda}_{roll_3}\right) \\ &\quad + \bar{\lambda}_{roll_5}\left(\bar{\lambda}_{roll_1} + \bar{\lambda}_{roll_2} + \bar{\lambda}_{roll_3} + \bar{\lambda}_{roll_4}\right) \\ G_4 &= -\left(\bar{\lambda}_{roll_1} + \bar{\lambda}_{roll_2} + \bar{\lambda}_{roll_3} + \bar{\lambda}_{roll_4} + \bar{\lambda}_{roll_5}\right) \end{aligned} \tag{72}$$

Proof. See Appendix A.

Remark 2. The pole–placement problem addressed by Theorem 1 is solved through the feedback of state variables characterizing the dynamics about the yaw, the roll, and the pitch axis. From a practical standpoint, rigid–body attitude and angular rate information are obtained as a typical output of the onboard Inertial Measurement Unit (IMU). On the converse, the estimation of payload oscillatory state is a challenging task that, however, was recently investigated by the one of the authors [19]. In particular, a method was validated to autonomously estimate the swing angle and angular rate in multicopter slung load applications, with no need to rely on sensors different from the available (typically low–cost) IMU. Accelerometer readings and dynamic model information can be fused by means of a Fading Gaussian Deterministic (FGD) filter, in the presence of model uncertainties and measurement errors, thus inferring full–state observability and controllability to $\bar{\boldsymbol{A}}_{roll}$ and $\bar{\boldsymbol{A}}_{pitch}$.

Remark 3. The FGD method outlined in Remark 2 is based on the assumption of a rigid cable with constant (nominal) length L, with the result that the estimation of oscillation angles and angular rates is uniquely related to the components of $\boldsymbol{\eta}_E$ and $\boldsymbol{\nu}_E$. On the converse, the elasticity of cable cannot be disregarded in the present framework and a residual degree of uncertainty characterizes the problem. From a practical standpoint, the use of sufficiently rigid cables drastically reduces model uncertainty, provided that $L_d \approx L$. From a theoretical standpoint, the vertical subsystem $\bar{\boldsymbol{A}}_v$ assumes a two–time–scale dynamic behavior: 1) multirotor motion along the local vertical represents a low–frequency mode observable through e_v and ε_v, with behavior principally determined by λ_{v_1}, λ_{v_2}, $\bar{k}_{i_h}$, and $\bar{k}_{p_h}$; 2) cable elongation dynamics, mostly observable through ν_{3_E} and η_{3_E}, which is representative of a high–frequency mode with properties strictly related to K and m_c. In this respect, the following Corollary is provided to investigate the frequency properties of $\bar{\boldsymbol{A}}_v$ and assign its closed–loop eigenvalues with an acceptable degree of accuracy.

Table 1
Multirotor slung–load system parameters.

Parameter	Symbol	Value	Units
Multirotor			
Mass	m	2.15	kg
Center of gravity position	$STA_{CG} = BL_{CG}$	0	m
	WL_{CG}	-0.02	m
Moments of inertia	J_1	0.0319	kg m^2
	J_2	0.0287	kg m^2
	J_3	0.0633	kg m^2
Center of pressure position	$STA_{CP} = BL_{CP}$	0	m
	WL_{CP}	-0.08	m
Frame drag areas	$A_1 = A_2$	0.023	m^2
	A_3	0.106	m^2
Propeller			
Number of blades	n_b	2	
Radius	R	0.1016	m
Mean aerodynamic chord	$\bar{c}$	0.0018	m
Chord @ 75% R	c_{75}	0.0021	m
Lift curve slope	a	5.9	rad^{-1}
Pre–cone angle	a_0	0	rad
Root pitch angle	θ_0	0.7854	rad
Total twist	θ_t	-0.6632	rad
Induced–power factor	k_{ind}	1.35	
Load			
Mass	m_c	0.5	kg
Reference area	A_c	0.008	m^2
Drag coefficient (sphere)	C_{dc}	0.5	
Cable			
Nominal cable length	L	0.6	m
Hookes's constant	K	4900	N/m
Hook point position	$STA_H = BL_H$	0	m
	WL_H	-0.1	m

Corollary 1. *Consider the decoupled subsystem matrix $\bar{\boldsymbol{A}}_v$ obtained in Theorem 1 and assume the control gains in Eq. (48) are selected as:*

$$\bar{k}_{i_v} = \frac{\Pi_v\,\delta_{fwd} - \bar{\Pi}_v\,\bar{\delta}_{fwd}}{2\,g\,n}, \quad \bar{k}_{p_v} = \frac{\bar{\Sigma}_v\,\bar{\delta}_{fwd} - \Sigma_v\,\delta_{fwd}}{2\,g\,n} \tag{73}$$

with $\bar{\Pi}_v = \bar{\lambda}_{v_1}\,\bar{\lambda}_{v_2}$ and $\bar{\Sigma}_v = \bar{\lambda}_{v_1} + \bar{\lambda}_{v_2}$. Then, the eigenvalues of $\bar{\boldsymbol{A}}_v$ approximately track $\bar{\lambda}_{v_1}$, $\bar{\lambda}_{v_2}$, $\bar{\lambda}_{v_3}$, and $\bar{\lambda}_{v_4}$ for sufficiently high values of K. Using standard notation [28], $\bar{\lambda}_{v_3}$ and $\bar{\lambda}_{v_4}$ are, in particular, characterized in terms of natural frequency and damping expressions as

$$\omega_f \approx \sqrt{K/m_c\,(1 + m_c/m)} \tag{74}$$

$$\omega_f\,\xi_f \approx -\bar{\Sigma}_v\,m_c/\,(2\,m) \tag{75}$$

Proof. See Appendix B.

4. Numerical results

In this Section, the validation of the proposed approach is addressed by numerical analysis. A DJI F550 Flamewheel hexarotor is considered, with relevant parameters listed in Table 1. The planar rotor configuration is characterized by $STA_{R_1} = STA_{R_6} = -STA_{R_3} = -STA_{R_4} = -0.2382$, $STA_{R_2} = STA_{R_5} = 0$ m, $BL_{R_1} = BL_{R_3} = -BL_{R_4} = -BL_{R_6} = 0.1375$ m, $BL_{R_2} = -BL_{R_5} = 0.2750$ m, and $WL_{R_j} = 0.0320$ m.

For the aim of the gain–sizing task, parameters $\bar{k}_T$ and $\bar{k}_Q$ in Assumption 1 are first evaluated on the basis of an experimental campaign performed at University of Bologna premises. In this respect, it must be noted that the data provided in Table 1 to perform nonlinear simulations already include model corrections based on the characterization tests described in what follows (see, for example, the induced–power factor, k_{ind}). Propulsion is provided by a set of DJI Opto 30A electronic speed regulators and DJI 2212 brushless motors powered by a 25C LiPo battery pack by Tattu with nominal voltage 14.8 V. Thrust is generated by DJI carbon–fiber reinforced nylon propellers with diameter $D = 8$ in and nominal pitch $\Gamma = 4.5$ in. The propulsion unit was mounted on a RCbenchmark Series 1585 thrust stand tailored to small and medium–size drone optimization analysis. The test bench supports thrust and torque measurement up to 5 kgf and 1.5 Nm, respectively, and an optical RPM probe for propeller angular rate estimation. Load cells are temperature–compensated and a preliminary calibration procedure allows for accurate measurements over the full operating range. Each experiment was conducted at room temperature $\tau_{exp} = 24\,^{\circ}$C and static pressure $p_{exp} = 100\,877$ Pa, with estimated air density $\rho_{exp} = 1.1827$ kg/m^3 and air dynamic viscosity $\mu_{exp} = 18.32 \cdot 10^{-6}$ Pa s. The PWM throttle signal was progressively incremented from $PWM_{idle} = 1100$ µs to $PWM_{max} = 2000$ µs (namely $\delta \in [0,\,900]^T$ µs), respectively generating zero and maximum thrust, with steady–state measurements taken at intervals of 100 µs.

In Fig. 4 the rotor angular rate Ω is reported as a function of control signal δ. Curve fitting of experimental data points is performed according to the model proposed in Eq. (10), with $k_\Omega = 14.92$ and $n = 0.6359$ (Root Mean Square Error, $RMSE = 13.65$ rad/s). In Fig. 5 the thrust T and the torque Q are depicted as a function of Ω. Data points are fitted according to the simplified models provided in Assumption 1, where $\bar{k}_T = 7.074 \cdot 10^{-6}$ N s/rad ($RMSE = 0.1276$ N) and $\bar{k}_Q = 1.326 \cdot 10^{-7}$ Nm s/rad ($RMSE = 0.0018$ Nm).

Consider now the isolated (unloaded) multirotor at 360 m altitude where, without loss of generality, $\chi \approx 1$ [26]. In the hovering condition it is $T_j = m\,g/6 = 3.514$ N and the feed–forward contribution to each motor results to be, according to Eq. (24), $\delta_{fwd} = 430$ µs. It is assumed that stabilization is performed by the sample inner controllers provided in Eqs. (26)–(29), with the control gains suggested in Eqs. (34)–(39). Let $\lambda_{v1} = -3.5 + i\,1.4$ and $\lambda_{v2} = -3.5 - i\,1.4$ be the desired (complex–conjugate) eigenvalues for an underdamped vertical dynamics, such that $\Pi_v = 14.21$ and $\Sigma_v = -7$. Required control gains result to be $k_{iv} = -489.35$ and $k_{p_v} = -241.06$. A critically–damped behavior is prescribed to the closed–loop yaw dynamics, such that $\lambda_{yaw_1} = \lambda_{yaw_2} = -3.5$, $\Pi_{yaw} = 12.25$, and $\Sigma_{yaw} = -7$. It follows $k_{ir} = 662.60$ and $k_{p_r} = 378.63$. With respect to the dynamics about the roll axis, one real pole and a pair of complex conjugate poles are assigned, respectively corresponding to $\lambda_{roll_1} = -5$, $\lambda_{roll_2} = -3.5 + i\,1.4$, and $\lambda_{roll_3} = -3.5 - i\,1.4$. Given $\Pi_{roll} = -71.05$, $\Xi_{roll} = 49.21$, and $\Sigma_{roll} = -12$, one derives $k_{i_\phi} = 132.01$, $k_{p_\phi} = 91.43$, and $k_p = -22.30$. In the case when, without loss of generality, the multirotor is to be provided with the same dynamic behavior about the roll and the pitch axes, namely $\lambda_{pitch_1} = \lambda_{roll1}$, $\lambda_{pitch_2} = \lambda_{roll2}$, and $\lambda_{pitch_3} = \lambda_{roll3}$, the remaining control gains can be scaled according to Eq. (39), such that $k_{i\theta} = 205.78$, $k_{p_\theta} = 142.53$, and $k_q = -34.76$.

The multirotor is equipped with a suspended load whose parameters are listed in Table 1. In the hovering condition it is $T_j = (m + m_c)\,g/6 = 4.33$ N, $L_d = 0.601$ m, and the feed–forward contribution to each motor is, according to Eq. (44), $\bar{\delta}_{fwd} = 506$ µs. Consider the dynamic system identified by the extended state vector in Eq. (47), under the hypotheses of Theorem 1. It is assumed, without loss of generality, that the auxiliary controllers in Eqs. (48)–(51) are required to provide $\bar{\lambda}_{yaw_1} = \lambda_{yaw_1}$,

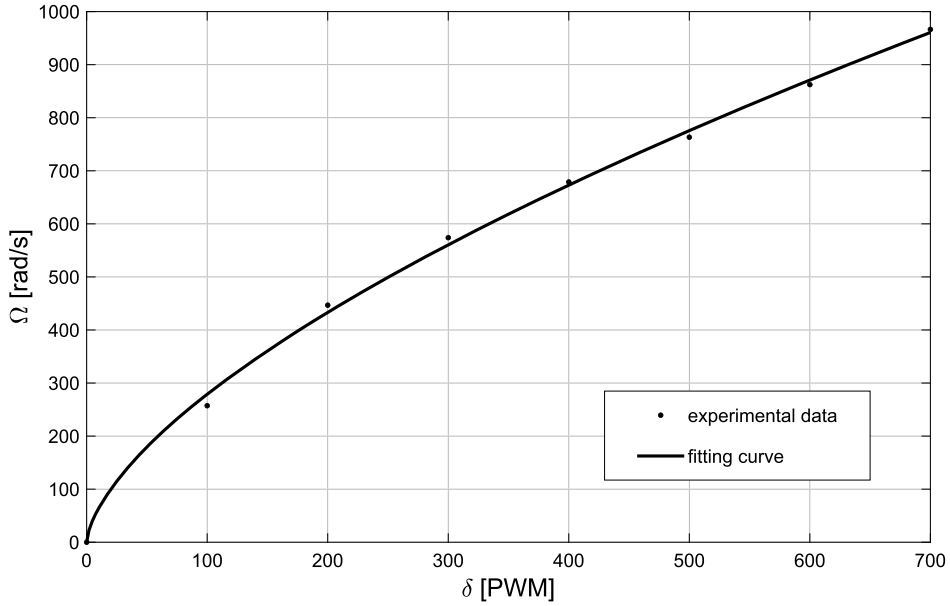

Fig. 4. DJI 8 × 4.5 propeller characterization (angular rate vs. PWM command).

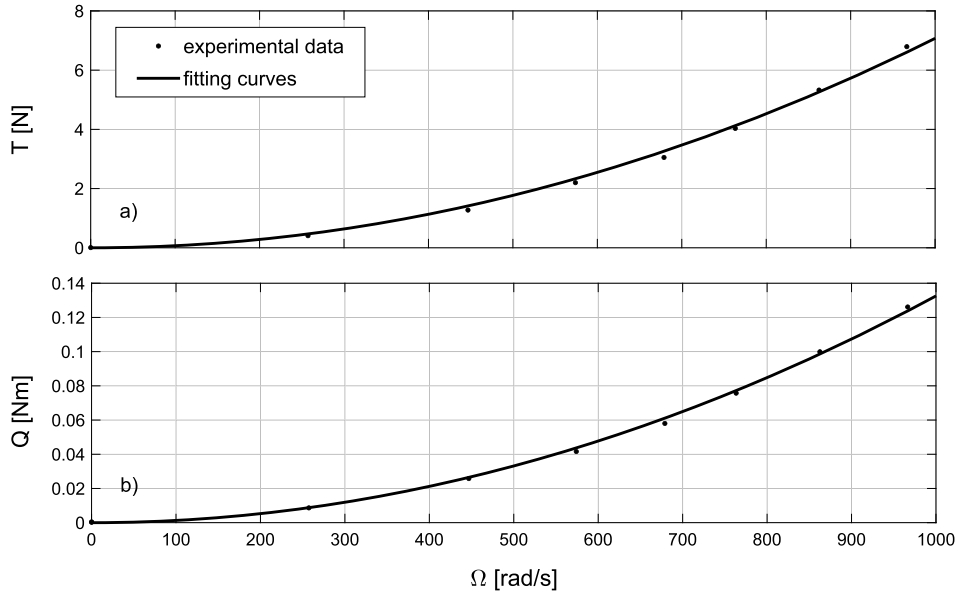

Fig. 5. DJI 8 × 4.5 propeller characterization (a) thrust and b) torque vs. angular rate).

$\bar{\lambda}_{yaw_2} = \lambda_{yaw_2}$, $\bar{\lambda}_{pitch_1} = \bar{\lambda}_{roll_1} = \lambda_{roll_1}$, $\bar{\lambda}_{pitch_2} = \bar{\lambda}_{roll_2} = \lambda_{roll_2}$, and $\bar{\lambda}_{pitch_3} = \bar{\lambda}_{roll_3} = \lambda_{roll_3}$. With regard to the dynamic mode connected to payload oscillation, a pair of complex–conjugate poles is prescribed, namely $\bar{\lambda}_{pitch_4} = \bar{\lambda}_{roll_4} = -1.2 + i\,1.7$ and $\bar{\lambda}_{pitch_5} = \bar{\lambda}_{roll_5} = -1.2 - i\,1.7$. As a first step, the parameters defined in Theorem 1 are evaluated, including $\Gamma = 1.0457$, $\Lambda = 0.0833$, and the polynomial coefficients $G_0 = 307.65$, $G_1 = 383.60$, $G_2 = 241.11$, $G_3 = 82.34$, and $G_4 = 14.40$. Given $\bar{\Pi}_{yaw} = \Pi_{yaw}$ and $\bar{\Sigma}_{yaw} = \Sigma_{yaw}$, control gains for the updated closed–loop yaw dynamics respectively follow from Eqs. (59)–(60) as $\bar{k}_{i_r} = -28.96$ and $\bar{k}_{p_r} = -16.55$. Control gains required for pole–placement stabilization of $\bar{\boldsymbol{A}}_{roll}$ are obtained from Eqs. (61)–(65) as $\bar{k}_{\eta_2} = 63.94$, $\bar{k}_{\nu_2} = 8.04$, $\bar{k}_{i_\phi} = -104.83$, $\bar{k}_{p_\phi} = -19.12$, and $\bar{k}_p = -2.49$. Taking into account Eqs. (66)–(69), control gains for closed–loop $\bar{\boldsymbol{A}}_{pitch}$ stabilization are, respectively, $\bar{k}_{\eta_1} = -91.80$, $\bar{k}_{\nu_1} = -12.53$, $\bar{k}_{i_\theta} = -163.42$, $\bar{k}_{p_\theta} = -34.53$, and $\bar{k}_q = -3.88$.

In order to highlight the effect of the auxiliary controller, it is assumed that the latter contribution is modulated by weight $\xi \in [0,\, 1]$, such that $\delta_{yaw} = \delta_{yaw}^{(inn)} + \xi\,\delta_{yaw}^{(aux)}$, $\delta_{roll} = \delta_{roll}^{(inn)} + \xi\,\delta_{roll}^{(aux)}$, and $\delta_{pitch} = \delta_{pitch}^{(inn)} + \xi\,\delta_{pitch}^{(aux)}$. The eigenvalues of subsystem matrices $\bar{\boldsymbol{A}}_{yaw}$ and $\bar{\boldsymbol{A}}_{roll}$ are depicted in Fig. 6 for values of ξ ranging from 0 to 1. In the case when $\xi = 1$, exact pole–placement occurs, based on given requirements. When $\xi = 0$, namely when the auxiliary controller does not provide contribution, rigid–body dynamics is shown to be altered by the presence of the suspended load. Concurrently, payload swing develops with a pair of poorly–damped poles, $-0.41 \pm i\,3.79$, characterized by a damping coefficient equal to 0.107 and natural frequency 2.45 rad/s. The effect of active payload stabilization, determined by $\bar{k}_{\eta_2}$ and $\bar{k}_{\nu_2}$, finally drives the poles of the swing mode to the desired values, $-1.2 \pm i\,1.7$, determining an improved damping ratio of 0.577, a natural frequency of 2.08 rad/s, and reduced settling time. The destabilizing effect de-

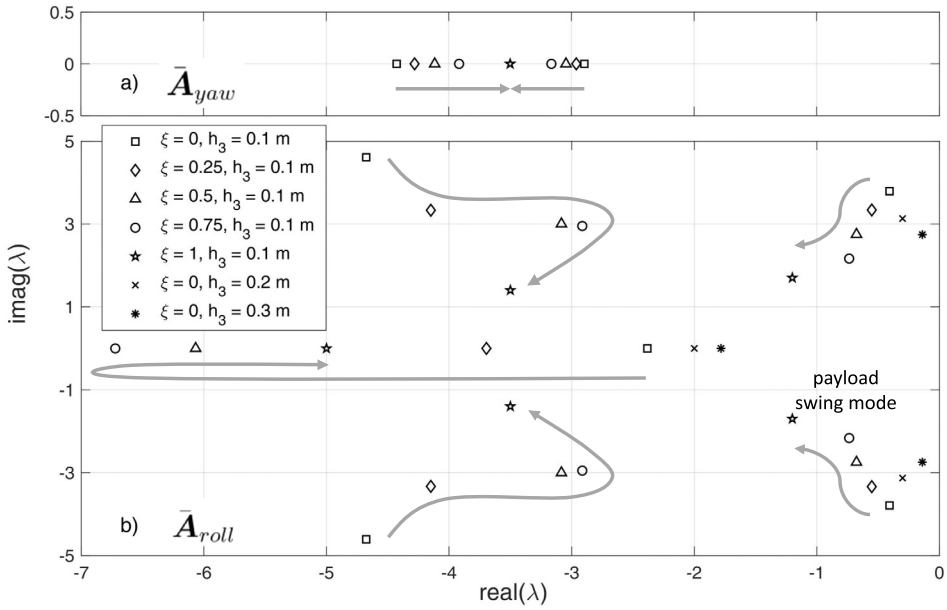

Fig. 6. The eigenvalues of a) $\bar{\boldsymbol{A}}_{yaw}$ and b) $\bar{\boldsymbol{A}}_{roll}$ respectively obtained for $\xi \in [0, 1]$.

termined by increasing values of h_3 is also evident. With regard to the yaw dynamics, the effect of the auxiliary controller arises in the transformation from real–distinct (over–damped) poles to the prescribed critically–damped poles, characterized by faster convergence.

Consider now the extended vertical dynamics. With the aim to provide the rigid body with almost the same dynamic behavior of the isolated multirotor, control gains are selected according to Eq. (73) in Corollary 1. In particular, it is $\bar{k}_{i_v} = -87.44$ and $\bar{k}_{p_v} = -43.08$, provided $\bar{\Pi}_v = \Pi_v = 14.21$ and $\bar{\Sigma}_v = \Sigma_v = -7$. Using standard notation [28] and the two–time–scale approach discussed in Appendix B, the resulting (rigid–body) slow mode is thus characterized in terms of natural frequency and damping expressions as $\omega_s = \sqrt{\bar{\Pi}_v} = 3.77$ rad/s and $\omega_s \xi_s = -\bar{\Sigma}_v/2 = 3.5$ rad/s. Conversely, the (cable elasticity) fast mode is described by expected values $\omega_f = \sqrt{K/m_c\,(1 + m_c/m)} = 109.90$ rad/s and $\omega_f \xi_f = -\bar{\Sigma}_v\, m_c/(2m) = 0.81$ rad/s. By substitution of the given control gains, $\bar{\boldsymbol{A}}_v$ assumes the form provided in Eq. (114), whose exact eigenvalues are identified by $\omega_s^{(exact)}$, $(\omega_s \xi_s)^{(exact)}$, $\omega_f^{(exact)}$, and $(\omega_f \xi_f)^{(exact)}$. In Table 2 percentage errors between exact and estimated dynamic parameters are reported as a function of cable Hookes's constant K, provided $\epsilon_{\omega_s} = \left(\omega_s - \omega_s^{(exact)}\right)/\omega_s^{(exact)} \cdot 100$, $\epsilon_{\xi\omega_s} = \left[(\xi_s\omega_s) - (\xi_s\omega_s)^{(exact)}\right] / (\xi_s\omega_s)^{(exact)} \cdot 100$, $\epsilon_{\omega_f} = \left(\omega_f - \omega_f^{(exact)}\right)/\omega_f^{(exact)} \cdot 100$, and $\epsilon_{\xi\omega_f} = \left[(\xi_f\omega_f) - (\xi_f\omega_f)^{(exact)}\right] / (\xi_f\omega_f)^{(exact)} \cdot 100$. It is evident that, for high values of K, frequency separation unfolds and the values estimated by Eqs. (110)–(113) reach a higher degree of accuracy, even though the analysis is limited to a zero dynamic residual $\boldsymbol{L} = \boldsymbol{L}_0$ in Eq. (105).

The proposed control strategy, tuned on the basis of a simplified linearized model, is finally validated by application to the full nonlinear simulator. To this end, 3 sample maneuvers (A, B, and C) are performed and a comparison is provided between obtained responses of both the linear and the nonlinear systems. In case A, the unloaded multirotor is assumed to be at hover with an initial non–null vertical velocity error, $e_v(0) = -1$ m/s, and $\varepsilon_v(0) = 0$ m. According to the given requirements, the response of linear vertical speed error is expected to represent an underdamped second–order system with maximum overshoot $S = 0.149$ m/s at time $t_o = 0.54$ s and settling time within 0.02 m/s range given by $t_s = 1.4$ s (solid black line in Fig. 7.a). Nonlinear simulation results from the same initial conditions (dashed black line in Fig. 7.a) provide $S = 0.152$ m/s (+2.01%) at time $t_o = 0.6$ s (+11.11%) and settling time $t_s = 1.46$ s (+4.29%). In case B, an initial yaw rate is considered such that $e_r(0) = -10$ deg/s and $\varepsilon_r(0) = 0$ deg. The linear subsystem yaw rate error is characterized by a maximum overshoot $S = 1.35$ deg/s at time $t_o = 0.57$ s and settling time within 0.02 deg/s range given by $t_s = 2.34$ s (solid black line in Fig. 7.b). Nonlinear simulation results from the same initial conditions (dashed black line in Fig. 7.b) provide $S = 1.46$ deg/s (+8.15%) at time $t_o = 0.64$ s (+12.28%) and settling time given by $t_s = 2.35$ s (+0.43%). In case C, with the aim to analyze the roll dynamics, the following initial conditions are considered: $p(0) = 0$ deg/s, $e_\phi(0) = -10$ deg, and $\varepsilon_\phi(0) = 0$ deg s. The time history of linear system error e_ϕ is detailed in Fig. 7.c (solid black line), where the maximum overshoot is $S = 2.63$ deg at $t_o = 0.72$ s and the settling time is $t_s = 2.38$ s. The rise time, here intended as the time interval between $0.9 \cdot e_\phi(0)$ and $0.1 \cdot e_\phi(0)$, is $t_r = 0.38$ s. With respect to the nonlinear system response (dashed black line in Fig. 7.c), corresponding results are $S = 3$ deg (+14.07%), $t_o = 0.72$ s ($\approx 0\%$), $t_s = 2.09$ s (−12.18%), and $t_r = 0.27$ s (−28.95%).

Consider now the loaded configuration under the effect of the inner and the auxiliary controllers while performing the same maneuvers A, B, and C. For the sake of brevity, the results of maneuvers B and C only are discussed. In Fig. 7.b the stabilization of yaw rate (maneuver B) is described while tracking almost exactly both the linear reference dynamics and the nonlinear unloaded model results (solid gray line). In this respect, it is $S = 1.42$ deg/s at time

Table 2
Extended vertical dynamics: evaluation of decoupled analysis approximation.

Hooke's constant [N/m]	approximation error [%]			
K	ϵ_{ω_s}	$\epsilon_{\xi\omega_s}$	ϵ_{ω_f}	$\epsilon_{\xi\omega_f}$
4.9	-11.04	-16.47	12.41	556.43
49	-3.13	-3.84	3.23	20.73
490	-0.33	-0.40	0.33	1.74
4900	-0.03	-0.04	0.03	0.17

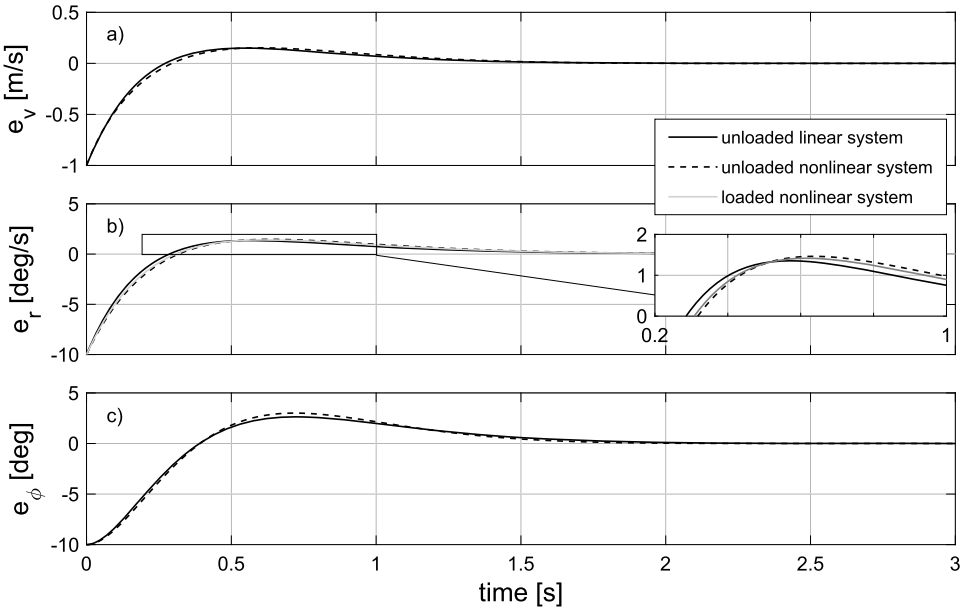

Fig. 7. Linear and nonlinear closed–loop system models (maneuvers A, B, and C).

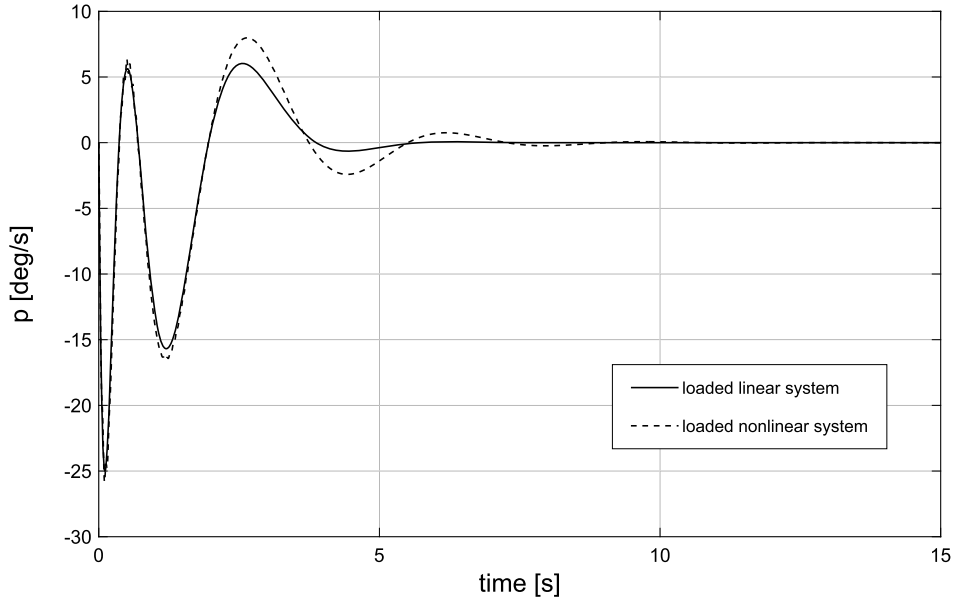

Fig. 8. Linear and nonlinear closed–loop system models (maneuver C).

$t_o = 0.62$ s and settling time is equal to $t_s = 2.37$ s. With regard to maneuver C, in Fig. 8 model comparison is performed on p, where the highly–nonlinear behavior related to the particular h_3 configuration rapidly emerges with time. Also, state variable η_{2H} is reported in Fig. 9 for $\xi = 0$ and $\xi = 1$, showing the efficacy of the auxiliary controller to stabilize multirotor dynamics while rapidly damping payload oscillations.

5. Conclusions

The present paper investigates the effects of suspended load oscillations on the dynamics of a multirotor platform. The isolated rotorcraft is first analyzed from a mathematical standpoint and a set of (inner–loop) controllers is assumed to stabilize the hovering condition with known dynamic behavior. Provided the vehicle is equipped with the payload through a suspended cable, the combined slung–load system is described as underactuated over the oscillatory dynamics. A set of auxiliary (outer–loop) controllers is thus proposed with the aim to provide the complete system with a set of desired dynamic properties, extended to the oscillatory modes. To this end, a completely analytical framework is derived to size the outer–loop controller gains according to the given requirements.

A numerical validation example is discussed relative to a small–scale hexacopter whose electric propulsion system is characterized experimentally. Although derived through a simplified set of linear equations, the proposed controller is proven to stabilize a highly–nonlinear multirotor model, while tracking the expected closed–loop behavior with satisfactory accuracy. As a by–product, results are also obtained that describe the effects of cable elasticity on system stabilization, showing how frequency separation phenomena characterize the vertical dynamics.

The approach, which has the merit of relative simplicity, can be extended to different rotorcraft configurations and requires the

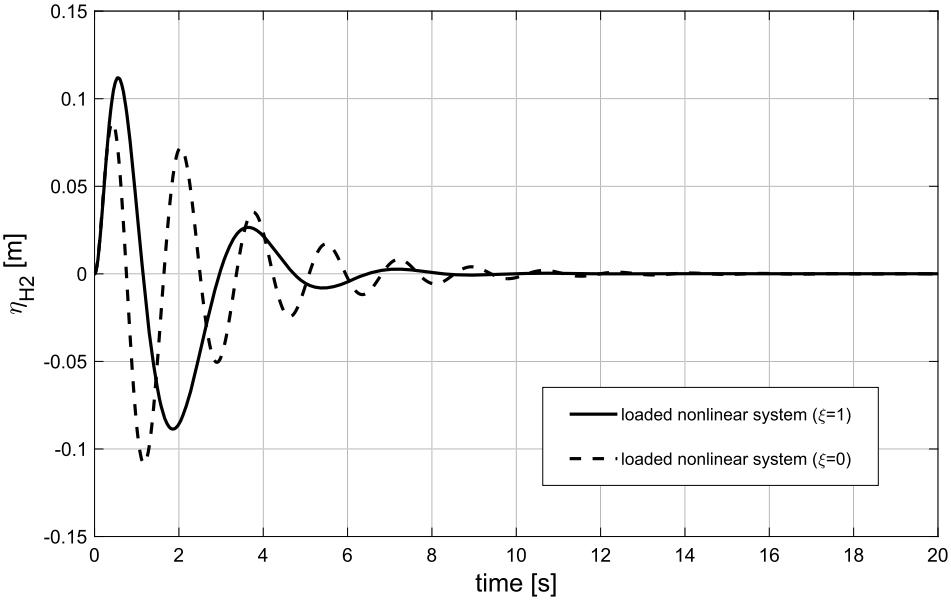

Fig. 9. The effect of auxiliary controller on payload stabilization (maneuver C).

knowledge of a very–limited set of vehicle parameters, while successfully encompassing the prescription of flying qualities.

Declaration of competing interest

The authors declare that they have no known competing financial interests or personal relationships that could have appeared to influence the work reported in this paper.

Data availability

No data was used for the research described in the article.

Appendix A. Proof of Theorem 1

The dynamic system identified by the extended state vector in Eq. (47) is first linearized about the origin. Under Assumptions 1–4, the state–matrix $\bar{\boldsymbol{A}} \in \mathbb{R}^{16\times 16}$ assumes the block–diagonal form provided in Eq. (52). In particular, the non–zero components of $\bar{\boldsymbol{A}}_v$ are:

$$\bar{A}_{v_{1,1}} = \frac{12\,k_T\,k_\Omega^2\,n\,\bar{\delta}_{fwd}^{2n-1}}{m}\left(\bar{k}_{p_v} + \frac{\Sigma_v\,\delta_{fwd}}{2\,g\,n}\right) \tag{76}$$

$$\bar{A}_{v_{1,2}} = \frac{12\,k_T\,k_\Omega^2\,n\,\bar{\delta}_{fwd}^{2n-1}}{m}\left(\bar{k}_{i_v} - \frac{\Pi_v\,\delta_{fwd}}{2\,g\,n}\right) \tag{77}$$

$$\bar{A}_{v_{1,4}} = K/m, \quad \bar{A}_{v_{3,4}} = -K/m_c\,(1+m_c/m) \tag{78}$$

$$\bar{A}_{v_{3,1}} = -\bar{A}_{v_{1,1}}, \quad \bar{A}_{v_{3,2}} = -\bar{A}_{v_{1,2}} \tag{79}$$

$$\bar{A}_{v_{2,1}} = \bar{A}_{v_{4,3}} = 1 \tag{80}$$

With respect to $\bar{\boldsymbol{A}}_{yaw}$, the following matrix components are derived:

$$\bar{A}_{yaw_{1,1}} = \Gamma\,\Sigma_{yaw} - \frac{2\,k_Q\,\bar{k}_{p_r}\,(m+m_c)\,g\,n}{J_3\,k_T\,\bar{\delta}_{fwd}} \tag{81}$$

$$\bar{A}_{yaw_{1,2}} = -\Gamma\,\Pi_{yaw} - \frac{2\,k_Q\,\bar{k}_{i_r}\,(m+m_c)\,g\,n}{J_3\,k_T\,\bar{\delta}_{fwd}} \tag{82}$$

$$\bar{A}_{yaw_{2,1}} = 1, \quad \bar{A}_{yaw_{2,2}} = 0 \tag{83}$$

By imposing the equations

$$\det\left[\bar{\boldsymbol{A}}_{yaw}\right] = -\bar{A}_{yaw_{1,2}} = \bar{\lambda}_{yaw_1}\,\bar{\lambda}_{yaw_2} = \bar{\Pi}_{yaw} \tag{84}$$

and

$$\mathrm{tr}\left[\bar{\boldsymbol{A}}_{yaw}\right] = \bar{A}_{yaw_{1,1}} = \bar{\lambda}_{yaw_1} + \bar{\lambda}_{yaw_2} = \bar{\Sigma}_{yaw} \tag{85}$$

the control gains in Eqs. (59) and (60) are respectively derived as the independent variables.

In a similar manner, the only non–zero components of $\bar{\boldsymbol{A}}_{roll}$ are:

$$\bar{A}_{roll_{1,1}} = \frac{2\,b\,(m+m_c)\,g\,n}{J_1\,\bar{\delta}_{fwd}}\left(\bar{k}_p + \frac{J_1\,\Sigma_{roll}\,\delta_{fwd}}{2\,b\,m\,g\,n}\right) \tag{86}$$

$$\bar{A}_{roll_{1,2}} = \frac{1}{J_1}\left[12\,b\,k_T\,k_\Omega^2\,n\,\bar{\delta}_{fwd}^{2n-1}\left(\bar{k}_{p_\phi} + \frac{J_1\,\Xi_{roll}\,\delta_{fwd}}{2\,b\,m\,g\,n}\right) - K\,h_3\,(L-L_d)\right] \tag{87}$$

$$\bar{A}_{roll_{1,3}} = \frac{m+m_c}{J_1\,m\,\bar{\delta}_{fwd}}\left(2\,b\,\bar{k}_{i_\phi}\,m\,g\,n - J_1\,\Pi_{roll}\,\delta_{fwd}\right) \tag{88}$$

$$\bar{A}_{roll_{1,4}} = \frac{12\,b\,k_{v_2}\,k_T\,k_\Omega^2\,n\,\bar{\delta}_{fwd}^{2n-1}}{J_1} \tag{89}$$

$$\bar{A}_{roll_{1,5}} = \frac{1}{J_1}\left[-\frac{K\,h_3\,(L-L_d)}{L_d} + \frac{2\,b\,k_{\eta_2}\,(m+m_c)\,g\,n}{\bar{\delta}_{fwd}}\right] \tag{90}$$

$$\bar{A}_{roll_{2,1}} = -1, \quad \bar{A}_{roll_{3,2}} = \bar{A}_{roll_{5,4}} = 1 \tag{91}$$

$$\bar{A}_{roll_{4,1}} = -h_3\,\bar{A}_{roll_{1,1}} \tag{92}$$

$$\bar{A}_{roll_{4,2}} = -\frac{h_3}{J_1}\left[\frac{2\,b\,(m+m_c)\,g\,n}{\bar{\delta}_{fwd}}\left(\bar{k}_{p_\phi} + \frac{J_1\,\Xi_{roll}\,\delta_{fwd}}{2\,b\,m\,g\,n}\right) - K\,h_3\,(L-L_d)\right] - \frac{(m+m_c)\,g}{m} \tag{93}$$

$$\bar{A}_{roll_{4,3}} = -h_3\,\bar{A}_{roll_{1,3}}, \quad \bar{A}_{roll_{4,4}} = -h_3\,\bar{A}_{roll_{1,4}} \tag{94}$$

$$\bar{A}_{roll_{4,5}} = \frac{K\,(L-L_d)}{J_1\,L_d\,m\,m_c}\left[J_1\,(m+m_c)+h_3^2\,m\,m_c\right] - \frac{2\,b\,h_3\,\bar{k}_{\eta_2}\,(m+m_c)\,g\,n}{J_1\,\bar{\delta}_{fwd}} \tag{95}$$

Provided $\bar{\lambda}_{roll_1}$, $\bar{\lambda}_{roll_2}$, $\bar{\lambda}_{roll_3}$, $\bar{\lambda}_{roll_4}$, $\bar{\lambda}_{roll_5}$ are the design eigenvalues, the desired characteristic polynomial of $\bar{\boldsymbol{A}}_{roll}$ assumes the form:

$$P_{roll}(s) = \prod_{i=1}^{5}\left(s-\bar{\lambda}_{roll_i}\right) = s^5 + G_4\,s^4 + G_3\,s^3 + G_2\,s^2 + G_1\,s + G_0 \tag{96}$$

where polynomial coefficients G_0, G_1, G_2, G_3, and G_4 are detailed in Eq. (72). Let $\boldsymbol{I}_5$ be the identity matrix of size 5. By equating the right–hand side of Eq. (96) to $\det\left[s\,\boldsymbol{I}_5 - \bar{\boldsymbol{A}}_{roll}\right]$, a set of 5 linear equations is derived with unknown variables represented by control gains $\bar{k}_{\eta_2}$, $\bar{k}_{\nu_2}$ $\bar{k}_{i_\phi}$, $\bar{k}_{p_\phi}$, and $\bar{k}_p$. Solutions are respectively given in Eqs. (61)–(65). The same procedure holds for $\bar{\boldsymbol{A}}_{pitch}$, finally providing the control gains in Eqs. (66)–(69).

Appendix B. Proof of Corollary 1

Taking into account Eqs. (76)–(80) in Appendix A, the vertical dynamics is conveniently rearranged into:

$$\bar{\boldsymbol{A}}_v = \begin{bmatrix} \boldsymbol{C}_{11} & \boldsymbol{C}_{12} \\ \boldsymbol{C}_{21} & \boldsymbol{C}_{22} \end{bmatrix} \tag{97}$$

where

$$\boldsymbol{C}_{11} = \begin{bmatrix} \bar{A}_{v_{1,1}} & \bar{A}_{v_{1,2}} \\ \bar{A}_{v_{2,1}} & 0 \end{bmatrix}, \quad \boldsymbol{C}_{12} = \begin{bmatrix} 0 & \bar{A}_{v_{1,4}} \\ 0 & 0 \end{bmatrix} \tag{98}$$

$$\boldsymbol{C}_{21} = \begin{bmatrix} \bar{A}_{v_{3,1}} & \bar{A}_{v_{3,2}} \\ 0 & 0 \end{bmatrix}, \quad \boldsymbol{C}_{22} = \begin{bmatrix} 0 & \bar{A}_{v_{3,4}} \\ \bar{A}_{v_{4,3}} & 0 \end{bmatrix} \tag{99}$$

Let $\boldsymbol{C}_0 = \boldsymbol{C}_{11} - \boldsymbol{C}_{12}\boldsymbol{C}_{22}^{-1}\boldsymbol{C}_{21}$. Provided $\boldsymbol{C}_{22}$ is nonsingular, the vertical dynamics equations are recast in the two–frequency–scale form [29]:

$$\dot{\boldsymbol{y}} = \boldsymbol{C}_{11}\,\boldsymbol{y} + \boldsymbol{C}_{12}\,\boldsymbol{z}, \quad \dot{\boldsymbol{z}} = \boldsymbol{C}_{21}\,\boldsymbol{y} + \boldsymbol{C}_{22}\,\boldsymbol{z} \tag{100}$$

where $\boldsymbol{y} = [e_v,\ \varepsilon_v]^T$ and $\boldsymbol{z} = \left[\nu_{3E},\ \eta_{3E}\right]^T$ are the vectors containing the slow/low–frequency and the fast/high-frequency variables, respectively. Consider the following change of variable:

$$\begin{bmatrix} \boldsymbol{y}_s \\ \boldsymbol{z}_f \end{bmatrix} = \begin{bmatrix} \boldsymbol{I}_2 - \boldsymbol{M}\,\boldsymbol{L} & -\boldsymbol{M} \\ \boldsymbol{L} & \boldsymbol{I}_2 \end{bmatrix} \begin{bmatrix} \boldsymbol{y} \\ \boldsymbol{z} \end{bmatrix} \tag{101}$$

where $\boldsymbol{I}_2$ is the identity matrix of size 2, while $\boldsymbol{L}$ and $\boldsymbol{M}$ are the solutions of the following matrix equations:

$$\boldsymbol{C}_{21} - \boldsymbol{C}_{22}\,\boldsymbol{L} + \boldsymbol{L}\,\boldsymbol{C}_{11} - \boldsymbol{L}\,\boldsymbol{C}_{12}\,\boldsymbol{L} = \boldsymbol{0}_2 \tag{102}$$

$$(\boldsymbol{C}_{11} - \boldsymbol{C}_{12}\,\boldsymbol{L})\,\boldsymbol{M} - \boldsymbol{M}\,(\boldsymbol{C}_{22} + \boldsymbol{L}\,\boldsymbol{C}_{12}) + \boldsymbol{C}_{12} = \boldsymbol{0}_2 \tag{103}$$

with $\boldsymbol{0}_2$ being the null matrix of size 2. The system in Eq. (100) is thus decoupled into the subsystems:

$$\begin{bmatrix} \dot{\boldsymbol{y}}_s \\ \dot{\boldsymbol{z}}_f \end{bmatrix} = \begin{bmatrix} \boldsymbol{C}_s & \boldsymbol{0}_2 \\ \boldsymbol{0}_2 & \boldsymbol{C}_f \end{bmatrix} \begin{bmatrix} \boldsymbol{y}_s \\ \boldsymbol{z}_f \end{bmatrix} = \begin{bmatrix} \boldsymbol{C}_{11} - \boldsymbol{C}_{12}\,\boldsymbol{L} & \boldsymbol{0}_2 \\ \boldsymbol{0}_2 & \boldsymbol{C}_{22} + \boldsymbol{L}\,\boldsymbol{C}_{12} \end{bmatrix} \begin{bmatrix} \boldsymbol{y}_s \\ \boldsymbol{z}_f \end{bmatrix} \tag{104}$$

Matrix $\boldsymbol{L}$ can be approximated as [29]:

$$\begin{aligned} \boldsymbol{L}_i &= \boldsymbol{C}_{22}^{-1}\,\boldsymbol{C}_{21} + \boldsymbol{C}_{22}^{-1}\,\boldsymbol{L}_{i-1}\,(\boldsymbol{C}_{11} - \boldsymbol{C}_{12}\,\boldsymbol{L}_{i-1}) \\ \boldsymbol{L}_0 &= \boldsymbol{C}_{22}^{-1}\,\boldsymbol{C}_{21} \end{aligned} \tag{105}$$

The existence of a solution to the matrix equality in Eqs. (102)–(103) and the validity of its approximation in Eq. (105) is addressed by Lemma 2.1 and Lemma 2.2 in [29]. If one selects a zero dynamic residual $\boldsymbol{L} = \boldsymbol{L}_0$ in Eq. (105) and takes into account Eq. (104), the approximations $\boldsymbol{C}_s^{(0)} = \boldsymbol{C}_{11} - \boldsymbol{C}_{12}\,\boldsymbol{C}_{22}^{-1}\,\boldsymbol{C}_{21}$ and $\boldsymbol{C}_f^{(0)} = \boldsymbol{C}_{22} + \boldsymbol{C}_{22}^{-1}\,\boldsymbol{C}_{21}\,\boldsymbol{C}_{12}$ can be derived:

$$\boldsymbol{C}_s^{(0)} = \begin{bmatrix} \bar{A}_{v_{1,1}}\left(\dfrac{m}{m+m_c}\right) & \bar{A}_{v_{1,2}}\left(\dfrac{m}{m+m_c}\right) \\ 1 & 0 \end{bmatrix} \tag{106}$$

$$\boldsymbol{C}_f^{(0)} = \begin{bmatrix} 0 & \bar{A}_{v_{3,4}}\dfrac{m_c}{m} \\ 1 & \bar{A}_{v_{1,1}}\left(\dfrac{m_c}{m+m_c}\right) \end{bmatrix} \tag{107}$$

Pole placement of $\bar{\lambda}_{v_1}$ and $\bar{\lambda}_{v_2}$ to the low–frequency subsystem matrix $\boldsymbol{C}_s^{(0)}$ is performed by the same approach adopted in Eqs. (84) and (85). Taking into account Eqs. (98) and (99), and the definition of $\bar{\Pi}_v$ and $\bar{\Sigma}_v$, it follows:

$$\bar{k}_{i_v} = \frac{\Pi_v\,\delta_{fwd} - \bar{\Pi}_v\,\bar{\delta}_{fwd}}{2\,g\,n} \tag{108}$$

and

$$\bar{k}_{p_v} = \frac{\bar{\Sigma}_v\,\bar{\delta}_{fwd} - \Sigma_v\,\delta_{fwd}}{2\,g\,n} \tag{109}$$

Using standard notation [28], the resulting low–frequency mode is characterized in terms of natural frequency and damping expressions as

$$\omega_s = \sqrt{\det[\boldsymbol{C}_s^{(0)}]} = \sqrt{\bar{\Pi}_v} \tag{110}$$

and

$$\omega_s\,\xi_s = -\operatorname{tr}[\boldsymbol{C}_s^{(0)}]/2 = -\bar{\Sigma}_v/2 \tag{111}$$

while the high frequency mode is related to

$$\omega_f = \sqrt{\det[\boldsymbol{C}_f^{(0)}]} = \sqrt{K/m_c\,(1+m_c/m)} \tag{112}$$

and

$$\omega_f\,\xi_f = -\operatorname{tr}[\boldsymbol{C}_f^{(0)}]/2 = -\bar{\Sigma}_v\,m_c/\,(2\,m) \tag{113}$$

Remark 4. By substitution of Eqs. (108) and (109), $\bar{\boldsymbol{A}}_v$ assumes the form:

$$\bar{\boldsymbol{A}}_v = \begin{bmatrix} \bar{\Sigma}_v\,(1+m_c/m) & -\bar{\Pi}_v\,(1+m_c/m) & & \\ 1 & 0 & 0 & 0 \\ -\bar{\Sigma}_v\,(1+m_c/m) & \bar{\Pi}_v\,(1+m_c/m) & 0 & -K/m_c\,(1+m_c/m) \\ 0 & 0 & 1 & 0 \end{bmatrix} \tag{114}$$

Since the eigenvalues of $\boldsymbol{C}_f^{(0)}$ cannot be arbitrarily assigned, matrix $\bar{\boldsymbol{A}}_v$ in Eq. (114) results to be generally characterized by different properties than the ones provided to the decoupled parameters in Eqs. (110)–(113). The matrix decomposition described above, in fact, allows to exactly perform pole placement only to the low–frequency dynamics while obtaining, as a by–product, the decoupled high–frequency mode parameters. However, the error between the coupled and the decoupled vertical dynamic modes is bounded and reduces in the measure in which frequency separation occurs. In this respect, the system in Eq. (100) does not need to be recast according to the singularly–perturbed form, in the presence of a small (explicit) parameter. Provided a sufficiently

rigid cable is used, that is a high value of K is considered, a sufficiently high natural frequency ω_f results for the subsystem in Eq. (112). Hence, inherent decoupling emerges and the eigenvalues of $\bar{\boldsymbol{A}}_v$ in Eq. (114) approximately track the results separately provided in Eqs. (110)–(113).

References

[1] M.D. Pavel, Understanding the control characteristics of electric vertical take–off and landing (eVTOL) aircraft for urban air mobility, Aerosp. Sci. Technol. 125 (2022) 1–9, https://doi.org/10.1016/j.ast.2021.107143.

[2] E.L. de Angelis, F. Giulietti, G. Rossetti, M. Turci, C. Albertazzi, Toward smart air mobility: control system design and experimental validation for an unmanned light helicopter, in: 48th European Rotorcraft Forum, 6–8 Sept. 2022, pp. 1–17.

[3] G. Avanzini, E.L. de Angelis, F. Giulietti, Optimal performance and sizing of a battery–powered aircraft, Aerosp. Sci. Technol. 59 (2016) 132–144, https://doi.org/10.1016/j.ast.2016.10.015.

[4] P.E.I. Pounds, D.R. Bersak, A.M. Dollar, Grasping from the air: hovering capture and load stability, in: Proc. of IEEE International Conference on Robotics and Automation, 9–13 May 2011, pp. 2491–2498, https://doi.org/10.1109/ICRA.2011.5980314.

[5] D. Zamerosky, G. Starr, J. Wood, R. Lumia, Rapid swing–free transport of nonlinear payloads using dynamic programming, J. Dyn. Syst. Meas. Control 130 (4) (2008) 1–11, https://doi.org/10.1115/1.2936384.

[6] K. Klausen, T.I. Fossen, T.A. Johansen, Nonlinear control with swing damping of a multirotor UAV with suspended load, J. Intell. Robot. Syst. 88 (2017) 379–394, https://doi.org/10.1007/s10846-017-0509-6.

[7] I. Palunko, R. Fierro, P. Cruz, Trajectory generation for swing–free maneuvers of a quadrotor with suspended payload: a dynamic programming approach, in: Proc. of IEEE International Conference on Robotics and Automation, 14–18 May 2012, pp. 2691–2697, https://doi.org/10.1109/ICRA.2012.6225213.

[8] F.A. Goodarzi, D. Lee, T. Lee, Geometric stabilization of a quadrotor UAV with a payload connected by flexible cable, Int. J. Control. Autom. Syst. 13 (6) (2015) 1486–1498, https://doi.org/10.1007/s12555-014-0304-0.

[9] K. Sreenath, T. Lee, V. Kumar, Geometric control and differential flatness of a quadrotor UAV with a cable–suspended load, in: Proc. of IEEE 52nd Annual Conference on Decision and Control, 10–13 Dec. 2013, pp. 2269–2274.

[10] M.M. Nicotra, E. Garone, R. Naldi, L. Marconi, Nested saturation control of an UAV carrying a suspended load, in: Proc. of American Control Conference, 4–6 June 2014, pp. 3585–3590, https://doi.org/10.1109/ACC.2014.6859222.

[11] J. Potter, W. Singhose, M. Costello, Reducing swing of model helicopter slung load using input shaping, in: Proc. of IEEE International Conference on Control and Automation, 19–21 Dec. 2011, pp. 348–353.

[12] G. Avanzini, A. Bottazzi, F. Giulietti, G. De Matteis, Accurate positioning of a payload suspended to a quadrotor unmanned aircraft, in: Proc. of 23rd Conference of the Italian Association of Aeronautics and Astronautics, 17–19 Nov. 2015, pp. 1–18.

[13] E.L. de Angelis, F. Giulietti, G. Pipeleers, Two–time–scale control of a multirotor aircraft for suspended load transportation, Aerosp. Sci. Technol. 84 (2019) 193–203, https://doi.org/10.1016/j.ast.2018.10.012.

[14] E.L. de Angelis, Stability analysis of a multirotor vehicle hovering condition, Aerosp. Sci. Technol. 72 (2018) 248–255, https://doi.org/10.1016/j.ast.2017.11.017.

[15] M.B. Tischler, System Identification Methods for Aircraft Flight Control Development and Validation, NASA Technical Memorandum, vol. 110369, 1995, pp. 1–22.

[16] PX4 Development Team and Community, PX4 autopilot user guide (main), https://docs.px4.io/main/en/. (Accessed 23 November 2021).

[17] E.L. de Angelis, G. Ferrarese, F. Giulietti, D. Modenini, P. Tortora, Gaussian deterministic recursive estimator with online tuning capabilities, J. Guid. Control Dyn. 38 (9) (2015) 1827–1833, https://doi.org/10.2514/1.G001024.

[18] E.L. de Angelis, G. Ferrarese, F. Giulietti, D. Modenini, P. Tortora, Terminal height estimation using a fading Gaussian deterministic filter, Aerosp. Sci. Technol. 55 (2016) 366–376, https://doi.org/10.1016/j.ast.2016.06.013.

[19] E.L. de Angelis, Swing angle estimation for multicopter slung load applications, Aerosp. Sci. Technol. 89 (2019) 264–274, https://doi.org/10.1016/j.ast.2019.04.014.

[20] P.D. Talbot, et al., A Mathematical Model of a Single Main Rotor Helicopter for Piloted Simulation, NASA Technical Memorandum, vol. 84281, 1982, pp. 1–52.

[21] Department of Defense, World Geodetic System 1984 - Its Definition and Relationship with Local Geodetic Systems, DMA Technical Report 8350.2, 1991, pp. 1–170.

[22] J.G. Leishman, Principles of Helicopter Aerodynamics, 2nd edition, Cambridge University Press, New York, 2006, Chs. 2 and 5.

[23] R.W. Deters, G.K. Ananda, M.S. Selig, Reynolds number effects on the performance of small–scale propellers, in: 32nd AIAA Applied Aerodynamics Conference, June 16–20 2014, pp. 1–43 https://doi.org/10.2514/6.2014-2151.

[24] G.D. Padfield, Helicopter Flight Dynamics, 2nd edition, Blackwell Pub., Oxford, 2007, Ch. 3.

[25] T.R. Scavo, J.B. Thoo, On the geometry of Halley's method, Am. Math. Mon. 102 (5) (1995) 417–426, https://doi.org/10.2307/2975033.

[26] U.S. Government Printing Office, U.S. Standard Atmosphere, NOAA-S/T 76-1562, Washington, D.C., 1976, pp. 1–241.

[27] E.L. de Angelis, F. Giulietti, G. Pipeleers, G. Rossetti, R. Van Parys, Two–time–scale control of a multirotor aircraft for suspended load transportation, Aerosp. Sci. Technol. 84 (2019) 193–203, https://doi.org/10.1016/j.ast.2018.10.012.

[28] D.T. McRuer, I. Ashkenas, D. Graham, Aircraft Dynamics and Automatic Control, Princeton University Press, Princeton, NJ, 1974, Ch. 5.

[29] P. Kokotović, H.K. Khalil, J. O'Reilly, Singular Perturbation Methods in Control: Analysis and Design, Society for Industrial and Applied Mathematics, Philadelphia, PA, 1999, pp. 49–54.